Theor. Comput. Fluid Dyn.
https://doi.org/10.1007/s00162-019-00513-y

ORIGINAL ARTICLE

Antoni Alomar · Aurélie Nicole · Denis Sipp ·
Valérie Rialland · François Vuillot

Reduced-order model of a reacting, turbulent supersonic jet based on proper orthogonal decomposition

Received: 8 December 2018 / Accepted: 28 December 2019

Abstract The present article deals with the spatiotemporal reduction of a reacting, supersonic, turbulent jet. A flowfield dataset is first obtained from a LES simulation including chemical reactions. The spatial reduction is accomplished by performing successively a Fourier transform in the azimuthal direction and a proper orthogonal decomposition (POD), while the temporal reduction is obtained through a selection of Fourier modes in the leading temporal POD modes (chronos). A prior low-pass temporal filter has been used to eliminate a significant portion of high-frequency content, the resulting reduced-order model (ROM) focusing only on the low-frequency, large-scale structures of the jet. The leading axisymmetric ($m = 0$) POD mode describes a very low-frequency pulsation of the shock cells. The second and third axisymmetric POD modes are paired and describe a wave packet amplified along the potential core and with a rapid decay downstream. The two leading helical ($m = 1$) POD modes, which are complex modes, appear to be mixed and together describe convecting wave packets of a longer wavelength and a lower frequency. They can be associated to the instability of the shear layer downstream of the potential core. Strong global cross-correlations are observed between the mass fractions and the axial velocity and temperature fields, which lead to similar energy decay rates and POD modes when they are included in the POD. The temporal reduction of the leading sets of chronos via an energy-based selection of Fourier modes has been shown to complement efficiently the spatial reduction, providing a complete spatiotemporal ROM of the flowfield.

Keywords Reduced-order model · Proper orthogonal decomposition · Turbulent jet · Reacting flows

1 Introduction

Aerodynamic flows play a fundamental role in the design of aerospace vehicles and related applications. At high Reynolds numbers, they can involve a high degree of complexity and require large amounts of computational resources to be simulated. In reacting flows, the aerodynamics problem is coupled to the reactions between the various chemical species, involving even larger amounts of information. From an experimental perspective, the continuous advancement of measuring techniques allows nowadays to perform time-resolved measurements

Communicated by Daniel J. Bodony.

A. Alomar (✉) · D. Sipp
DAAA, ONERA, Université Paris-Saclay, 92190 Meudon, France
E-mail: tonignasi@gmail.com

A. Alomar · A. Nicole · F. Vuillot
DMPE, ONERA, Université Paris-Saclay, 91123 Palaiseau, France

V. Rialland
DOTA, ONERA, Université Paris-Saclay, 91123 Palaiseau, France

Published online: 09 January 2020

of large spatial regions, the most relevant example being particle image velocimetry. So in both the numerical and the experimental fields, increasingly large computational resources are required. In this situation, reduced-order models (ROMs) of the flowfield are particularly useful. ROMs are models that mimic the behavior of the original flowfield, but using less information. The two general defining properties of a ROM are (1) that it reduces the size (in terms of amount of information), and (2) that it provides accurate approximations of the original system. These two requirements are incompatible to a certain extent, and therefore a compromise between them is needed. Focusing the ROM onto specific aspects of the system is an important advantage. Beside the size reduction, which leads to a cheaper and faster manipulation, ROMs are a powerful tool to decompose complex systems into simpler mechanisms, providing additional insight into the physics of the system.

Supersonic reacting jets out of design conditions appear commonly in space launchers and missiles. The large changes in altitude experienced by these vehicles induce large changes in the exit pressure, leading to over-expansion (low-altitude) or under-expansion (high-altitude) conditions. In certain configurations the jets are reacting, i.e., there exist chemical reactions in the flowfield, typically driven by the mixing and combustion between a fuel and an oxidant. The resulting flame interacts with the flow through the generation of heat. At the same time, the flame generates electromagnetic radiation peaking in the infrared, which can be used for detection purposes. The continuous advances in computational capabilities allow nowadays to perform high-fidelity simulations of such complex flows, which not only can account for the large number of spatial degrees of freedom associated with turbulent flows, but also for the additional equations and flow variables required to describe the chemical reactions. In the present study, a turbulent, reacting supersonic jet out of design conditions obtained from a LES simulation including all relevant chemical reactions has been considered as a test case to assess a spatiotemporal ROM.

The spatial reduction of the ROM has been achieved by proper orthogonal decomposition (POD). POD is a statistical tool based on an eigenvalue decomposition of the flowfield auto-correlation function. A fundamental property of POD is that the N-th rank reconstruction is the best linear approximation of rank N of the original flowfield, in terms of total variance, and with respect to a given scalar product. The choice of scalar product certainly carries arbitrariness, but at the same time also flexibility to focus on particular variables or regions of interest. This makes POD an efficient tool to build ROMs, by simply taking a reduced set of leading POD modes. In many flows, a small number of POD modes are sufficient to reconstruct the most energetic coherent structures [1,2]. When the flow exhibits a periodic direction the initial POD analysis can be decoupled into lower dimensional POD problems through a Fourier transform along that direction [3]. In such cases, POD leads to an even more efficient reduction [4,5].

Various methods have been proposed in the past to obtain temporal ROMs of aerodynamic flows. A physics-based temporal ROM results from projecting the Navier–Stokes equations onto a reduced POD basis (POD-Galerkin method). This leads to a temporal differential system governing the amplitude of the different POD mode amplitudes. This approach is capable of capturing the dynamical behavior of a number of flows [6], but it can lead to non-physical behavior and numerical instabilities at high Reynolds numbers due to the miss-modeling of the energy transfer to the small scales [7]. Additional modeling for the neglected low-energy modes is then required (see for example [8]). Another physics-based approach to obtain temporal ROMs, which has had success for moderate Reynolds numbers, consists in modeling the flow from a low-rank approximation of the resolvent operator [9–11] around the mean flow. The success of the resolvent operator approach together with a linearization around the mean flow has been clarified by [12].

The previous temporal ROMs work well at low and moderate Reynolds numbers, and they are intimately linked to the inherent dynamics of the flow. However, due to their fundamental inability in accounting for the strongly nonlinear dynamics of the turbulent scales, they fail at high Reynolds numbers. In this regime, empirical approaches are required. Dynamic mode decomposition (DMD) is an algorithm leading to the optimal low-order linear approximation of the flow dynamics, from a set of snapshots of the flow [13,14]. Chen et al. [15] showed that DMD is equivalent to a discrete Fourier transform when applied to mean-removed data. Cammilleri et al. [16] proposed applying DMD to the entire chronos basis (chronos-DMD). In this case, the limitation of conventional DMD of determining at most an incomplete basis of dynamic modes disappeared, as the dimension of the chronos vectors can be made equal to the number of snapshots, if all the POD modes are computed. In fact, chronos-DMD requires the entire basis of chronos if all the snapshots are included; otherwise, it leads to unstable dynamic modes and large reconstruction errors. But with datasets containing long series of snapshots, the calculation of all the POD modes may be computationally expensive. Another well-known empirical approach leading to a temporal ROM consists of fitting the chronos to a polynomial differential system via a least-squares method [17]. This approach can prevent the numerical instabilities found in POD-Galerkin and is *a priori* applicable to arbitrary Reynolds numbers. If the nonlinear terms are neglected, the resulting differential system can be transformed to an algebraic system in the frequency domain, preventing the need of estimating the time derivatives numerically. A further reduction can be obtained by retaining a limited set of Fourier modes. The resulting Fourier-based temporal ROM has been considered in the present study.

Another fundamental aspect of POD is that the POD modes are statistically coherent motions of the flow. This property was the motivation in the original use of POD in fluid mechanics [18]. An unforced turbulent jet is a complex dynamical system involving a broad range of scales, from large coherent structures to small-scale turbulence. The study of the coherent structures from experiments or simulations is difficult because they are superposed to the small-scale motions. The situation is worse at higher Reynolds numbers because the energy associated with the former diminishes with respect to the latter [4]. In these conditions, POD remains a useful tool to extract large-scale coherent motions. Due to its generality, POD can be used in complex flowfields, such as flowfields including chemical reactions. POD has been successfully used to study the energetically dominant coherent structures of low and moderate Reynolds number reacting jets [2,19].

The goal of the present study is the building of a general, flexible and stable spatiotemporal ROM for the large, approximately linear scales of stationary flows. Simultaneously, the ROM is used to explore the energetically dominant modes. A spatial reduction is performed by a POD truncation, and a temporal reduction by selecting a set of dominant temporal Fourier modes. The ROM is built exclusively from the retained topos and chronos basis. Unlike previously proposed ROMs based on POD, here the stationarity of the flow is exploited through the use of a temporal Fourier basis. Also, the temporal ROM is determined by a global fit, instead of the local first derivatives of the chronos, as in Perret et al. [17]. On the other side, the proposed ROM is not appropriate to model transitory solutions, for which other approaches [13,17] are preferable. In order to illustrate its generality, the ROM has been applied to a demanding test case: a turbulent, reacting, imperfectly expanded jet. The purpose of the ROM is modeling the infrared radiation emitted by the jet [20]; thus, the flow variables, the spatial region, the range of frequencies, etc., are set accordingly.

The structure of the manuscript is as follows. First, the flowfield considered as test case is presented, including the simulation and extracted dataset, the mean flow, the frequency and azimuthal content and the low-pass filter. The spatial reduction is then addressed, including the POD algorithm and the POD results corresponding to two sets of variables, one without and one with selected species mass fractions. Finally, the temporal reduction for sets of leading chronos is presented corresponding to the complete set of variables of interest, and the resulting spatiotemporal ROM is assessed.

2 Reacting supersonic jet: presentation of the LES simulation

The jet is generated by an upstream combustion chamber, where the reaction between oxygen (GOX) and methane (GCH_4) occurs. The combustion chamber communicates to the ambient through a convergent-divergent nozzle, with a geometrical expansion ratio of 2.37 (nozzle exit area divided by throat area). The simulation geometry and boundary conditions resemble the 'MASCOTTE' combustion facility at ONERA. Figure 1 shows the simulation geometry and the boundary conditions imposed. The flow domain is axisymmetric. The ambient pressure ($P_\infty = 101{,}325$ Pa) is imposed at the downstream boundary. The lateral boundary consists of a velocity inlet, where a low velocity parallel to the jet axis ($U_\infty = 5$ m/s) is imposed, together with the temperature ($T_\infty = 288.15$ K) and the mass fractions ($Y_{O2} = 0.23$, $Y_{N2} = 0.77$) in ambient conditions. The jet inlet corresponds to a downstream section of the combustion chamber, where the chemical reactions have been completed and the velocity is close to zero. A stagnation inlet boundary condition is imposed, defined by the chamber temperature ($T_{cc} = 2400$ K), pressure ($P_{cc} = 850{,}000$ Pa), and the mass fractions of the combustion products ($Y_{H2} = 0.06$, $Y_{\mathrm{H2O}} = 0.28$, $Y_{\mathrm{CO}} = 0.57$, $Y_{\mathrm{CO2}} = 0.09$). All wall boundaries (thick solid line in Fig. 1) are adiabatic. The boundary layer on the nozzle walls is modeled using wall functions. Based on the conditions at the section $x = 0.2D$, where the mean flow is approximately uniform, the jet is weakly over-expanded, with an exit pressure of 0.74 times the ambient pressure, an axial velocity of 2290 m/s, a temperature of 1450 K and a Mach number of 2.15. The exit Reynolds number based on ambient conditions is 3,600,000.

The origin of both the cylindrical and Cartesian coordinates used is at the center of the nozzle exit. The velocity, temperature and pressure have been normalized with the values immediately upstream of the normal shock ($x = 0.85D$): $U_J = 2750$ m/s, $T_J = 953$ K and $P_J = 6404$ Pa. There the velocity and the pressure attain their maximum and minimum values, respectively. The frequency is non-dimensionalized through the Strouhal number, $\mathrm{St} = f D/U_J$.

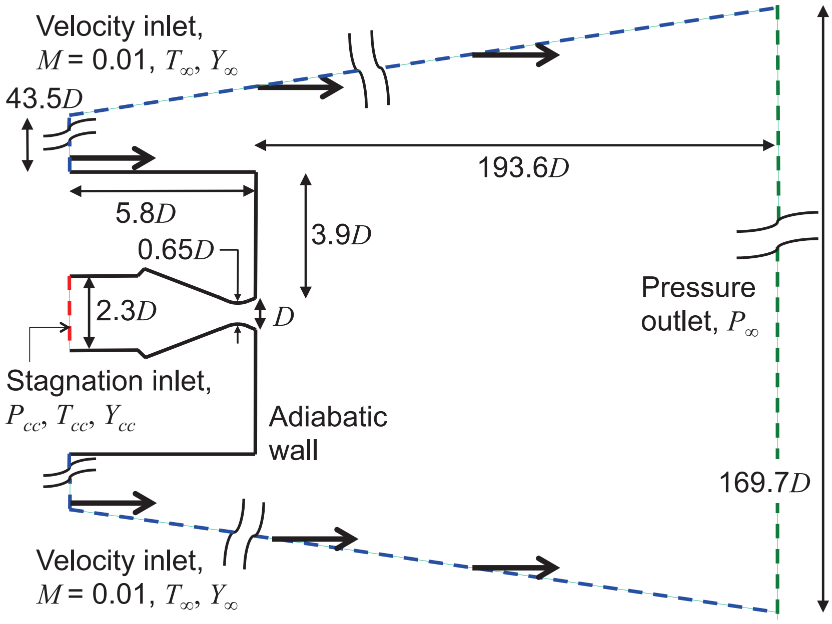

Fig. 1 Sketch of the geometry of the simulation and the boundary conditions

The simulation has been performed with the multi-physics code CEDRE, developed at ONERA. This code has been applied with success to hot supersonic jets [21] and reacting supersonic jets [20,22,23]. Details of the code, and a review of its capabilities and particular applications can be found in [24]. The code uses a second-order finite volume discretization (first order at the boundaries). In this particular case, a multi-slope interpolation scheme has been used [25]. The numerical fluxes are computed by the HLLC approximation Riemann solver with contact discontinuity [26]. No additional dissipation or entropic corrections are imposed. Time is discretized through a second-order, implicit Runge–Kutta scheme.

All species are treated as ideal gases with heat capacities varying with temperature. They form a perfect mixture in local thermal equilibrium. For each species k: $P_k = \rho_k R_k T$, $P_k = X_k P$, $Y_k = \mu_k X_k/(\sum \mu_l X_l)$. For the mixture: $\sum P_k = P$, $\sum X_k = \sum Y_k = 1$, $P = \sum \rho_k R_k T = \rho R T$ (R_k and R are the species and the mixture specific gas constant, respectively, X_k is the molar fraction, Y_k is the mass fraction, and μ_k is the molar mass). The reaction rates are modeled by Arrhenius equations.

The jet is assumed to be fully turbulent, and the classical Smagorinsky subgrid model has been used with constants $C = 0.1$, $C_\mu = 0.09$. A re-combustion flame spontaneously appears and grows along the shear layer, generated by the interaction of the hydrogen and the carbon monoxide ejected by the jet with the oxygen in the ambient. This turbulent diffusion flame should strictly be modeled with account of chemistry subgrid-scale model coupling [27–29]. As a first approximation, it has been assumed that the chemical reactions and the turbulence subgrid-scale model are uncoupled. This implies that the reaction occurs as if the flow was locally laminar, and also that the flame has no effect on the subgrid-scale model. This is likely not an accurate approximation everywhere in the flow domain, but is deemed a reasonable first approach.

An unstructured, isotropic tetrahedral mesh has been used. It is refined at the nozzle walls and in the vicinity of the nozzle exit, and then progressively coarsened downstream and in the radial direction away from the shear layer. At the nozzle lip, the cell size is $0.01D$. Along the lip line, the cell size increases from $0.01D$ to $0.03D$, at $x = 5D$, and to $0.06D$ at $x = 12D$. Along the jet axis, the cell size goes from $0.025D$, at the nozzle exit, to $0.03D$ at $x = 5D$, and to $0.06D$ at $x = 12D$. The LES mesh quality index introduced by Celik et al. [30] has been checked to be higher than 75% in the mixing layers and the self-similar region, indicating an adequate resolution.

The simulation time step is 10^{-7} s, which allows a proper resolution of all chemical reactions involved. The total simulation time was 0.01925 s, corresponding to 77 runs of 2500 time steps per run. The flow was started from a RANS solution with the same mesh and boundary conditions. It took an initial transient of about 0.008 s for the flow to become statistically stationary. The snapshot sampling and the calculation of the mean flow carried on during 0.01125 s of simulation time, which corresponds to 1750 convective times ($1750D/U_J$).

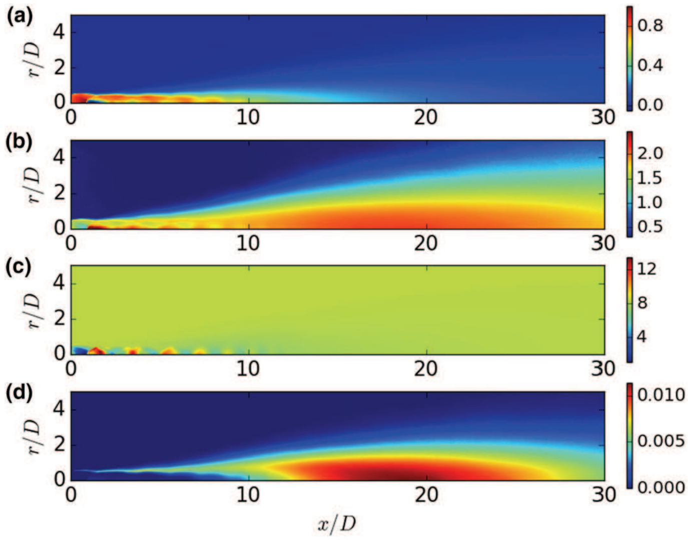

Fig. 2 Colormaps of **a** the mean axial velocity, U_0/U_J, **b** mean temperature, T_0/T_J, **c** mean pressure, P_0/P_J and **d** mean mass fraction of OH, $Y_{OH,0}$

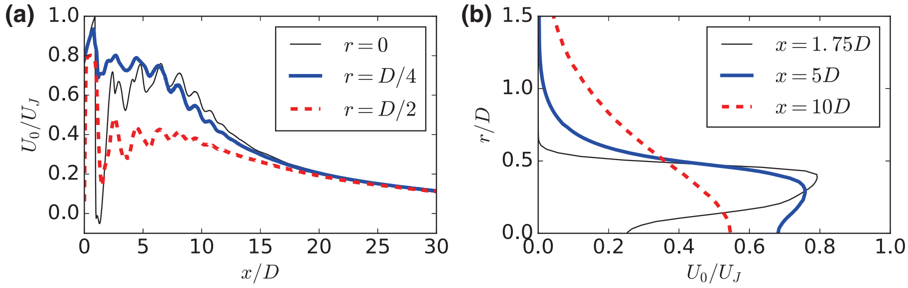

Fig. 3 **a** Mean axial velocity along the jet at various distances from the axis and **b** axial velocity profiles at various distances from the nozzle exit

The mean flowfields of the axial velocity, temperature, pressure and mass fraction of OH are shown in Fig. 2a–d, respectively. The potential core region of imperfectly expanded supersonic jets contains an approximately periodic series of shock cells, which can be appreciated in Fig. 2a–c. This can also be observed in Fig. 3a, where the axial velocity along the jet at various distances from the jet axis is shown. The shock cells weaken toward the downstream direction until the flow is subsonic everywhere. The length of the first shock cell is about $1.47D$, somewhat higher than $1.23D$, the value obtained from the inviscid model of [31] (although strictly Pack's model is valid in the vicinity of $M \approx 1$). A similar difference with the inviscid solution was obtained by [32] for a LES simulation of an over-expanded jet. As expected in conditions of over-expansion, there is a normal shock within the first shock cell, which is located at $x \approx 0.9D$. The normal shock induces a re-circulation immediately downstream and a strong decrease of the velocity along the jet axis (Fig. 3b). As observed in Fig. 2b, the mean temperature strongly increases downstream. This is due to the re-combustion flame that appears first within the shear layer, and then spreads through the entire jet. It can be visualized in Fig. 2d through the mass fraction of OH. It has been checked that the velocity components follow the self-similarity laws expected at high Reynolds numbers, downstream of $x \approx 10D$. A recent study has shown that the state of the boundary layer at the nozzle exit can have an impact on the growth rate of the wave packets in the vicinity of the nozzle, and on the radiated noise [33]. In general, the accuracy of the spatiotemporal ROM will depend on the accuracy of the underlying simulated data-base. The CFD simulation performed in this study was a first approach on this particular flow, and efforts are already being made to improve this crucial feature in future attempts [34,35].

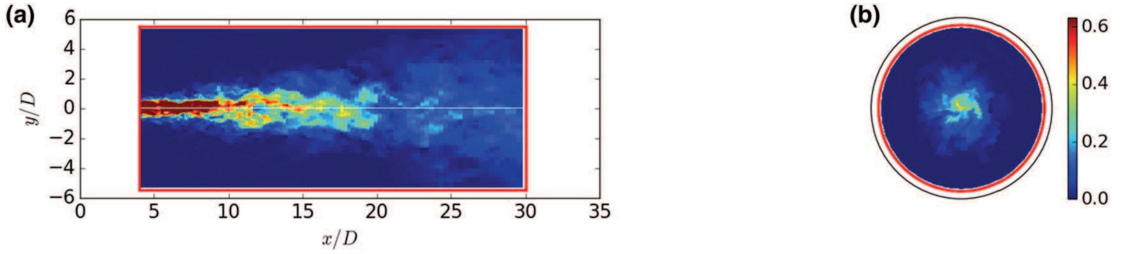

Fig. 4 **a** Axial slice and **b** normal slice illustrating the region of the ROM (colormap of a snapshot of axial velocity, normalized by U_J)

3 Objective of ROM

3.1 Flow region of interest for the ROM

The size and location of the spatial region considered for the POD analysis is determined by the requirements of the ROM. In the present test case, the goal is to compute the infrared radiation emitted by the jet. It is then necessary to capture the high temperature and mass fraction fields of the chemical species, which extend well downstream of the potential core. A cylindrical region has been considered: $4D < x < 30D$, $r < 6D$. It is shown in Fig. 4, the colormap representing the axial velocity. The considered region contains a portion of the potential core ($4D < x < 8D$), the transition region ($8D < x < 12D$) and the self-similar region ($12D < x < 30D$). Neglecting the sector $x < 4D$ significantly reduces the region size in terms of number of cells, therefore reducing the data matrices and the memory requirements (a parallel computation of the auto-correlation matrices directly from the simulation was not available). Unless the interest is limited to a particular spatial region, it is important that the latter is as large as possible to assure that most of the fluctuating energy is accounted for. The three-dimensional sampling grid is formed of $N_x = 135$ axial points, $N_r = 50$ radial points and $N_\theta = 36$ azimuthal points. The density of grid points diminishes downstream and is maximum on $r = D/2$.

3.2 Frequency content of interest for the ROM

In this section, we first analyze the frequency content along the jet and estimate the required sampling frequency to avoid aliasing in time (Sect. 3.2.1). We then introduce a low-pass filtering onto the gathered snapshots to focus on the frequency band of interest for our ROM (Sect. 3.2.2).

3.2.1 Frequency and azimuthal content along the jet

The active frequencies along the jet have been assessed through a number of sensors along the shear layer. Figure 5a–c shows the energy spectrum of the axial velocity signal measured at $x = 5D$, $x = 10D$ and $x = 20D$, respectively. Within the potential core, the spectrum displays a peak at St ≈ 0.2, which progressively shifts to lower frequencies downstream. At $x = 20D$, the peak is located around St ≈ 0.03. Similar trends are observed for the other flow variables.

Since no pre-filtering of the simulated field has been applied, the sampling frequency of the snapshots needs to be high enough to maintain the aliasing low. At the same time, the total number of extracted snapshots is limited by simulation time and data size constraints. In the present case, a sampling frequency of $\mathrm{St_{samp}} = 1.12$ has been deemed a good compromise. The corresponding Nyquist frequency, $\mathrm{St_{Nyq}} = \mathrm{St_{samp}}/2$, is shown in Fig. 5a–c (solid vertical lines). The area under the spectra for frequencies higher than the Nyquist frequency is much lower than the area at lower frequencies, which implies that the aliasing is weak. Note also that the spectrum shifts to lower frequencies downstream, diminishing the aliasing even further. If pre-filtering of the simulated field had been applied, one would have more freedom in the determination of the sampling frequency of the snapshots. It could directly be set as twice the maximum frequency of interest for the ROM.

The evolution of the azimuthal spectrum along the jet is presented in Fig. 6. Similarly to non-reacting turbulent jets, in the upstream region the azimuthal spectrum is highly distributed among the 10 leading azimuthal modes, and the spectrum shifts to lower order modes downstream. As opposed to the velocity, the leading azimuthal modes of the temperature are more intense downstream than upstream, due to the flame.

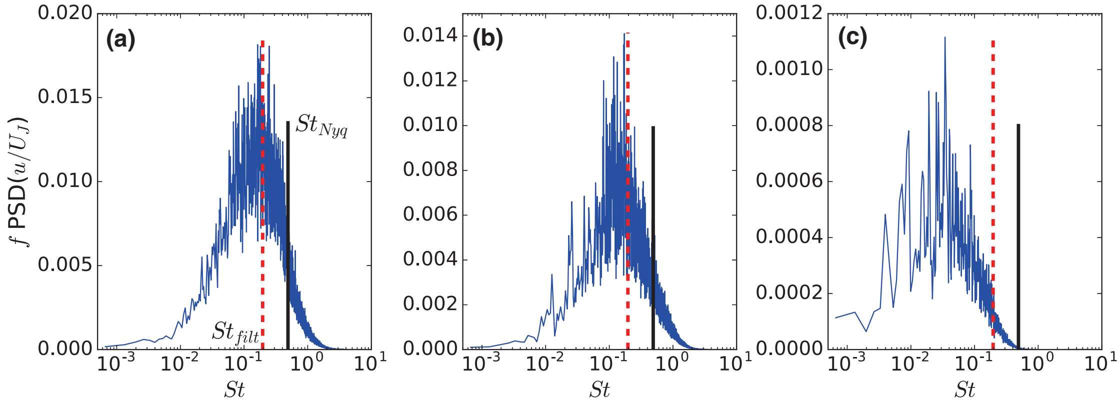

Fig. 5 PSD of the axial velocity fluctuations at **a** $x = 5D$, **b** $x = 10D$ and **c** $x = 20D$, on the jet lip line ($r = D/2$). The vertical lines show the Nyquist frequency (solid line) and the cutoff frequency of the low-pass filter (dashed line)

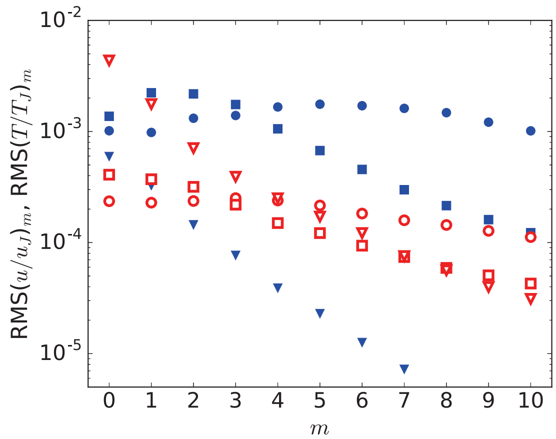

Fig. 6 Azimuthal spectrum of the axial velocity (filled) and the temperature (empty) along the jet, at $x = 5D$ (circles), $x = 10D$ (squares) and $x = 20D$ (gradients)

3.2.2 Low-pass temporal filter

A low-pass temporal filter has been applied prior to performing the spatial and temporal reductions. In the presented test case, we have chosen to focus on the larger scales of the jet, and this is the goal of the low-pass temporal filter. A linear ROM cannot be expected to model efficiently the entire range of scales present in a high Reynolds number flow, and especially the small scales, such as those involved in the turbulent cascade. Only the large structures can be efficiently reduced and are of interest for the applications mentioned in this article. Nevertheless, should the interest be on higher frequencies, the cutoff frequency can be increased as wished. A cutoff frequency $\mathrm{St}_{\mathrm{filt}} = 0.4\mathrm{St}_{\mathrm{Nyq}}$ has been used (dashed vertical lines in Fig. 5a–c). This frequency is too low to resolve a significant portion of the energy spectrum in the potential core region, but it is high enough to capture the vast majority of the energy downstream. Overall, the filter removes a 16% of the total energy for the ensemble of the pressure, temperature and velocity components.

Figure 7 highlights the impact of the filter on a snapshot of temperature. The filter effect is very weak away from the upstream jet core, where the mean velocity is higher and the fluctuations are fastest. The filter used is a Chebyshev type II filter of order 5, with a 40 dB attenuation imposed at the stop band. The coefficients of the filter can be obtained from the *Python* library *scipy.signal*.

4 Spatial reduction with POD

The spatial reduction of the ROM is achieved by a POD method. First, the fundamentals of POD are summarized (Sect. 4.1), including the use of a scalar product to focus the reduction on some specific variables, the

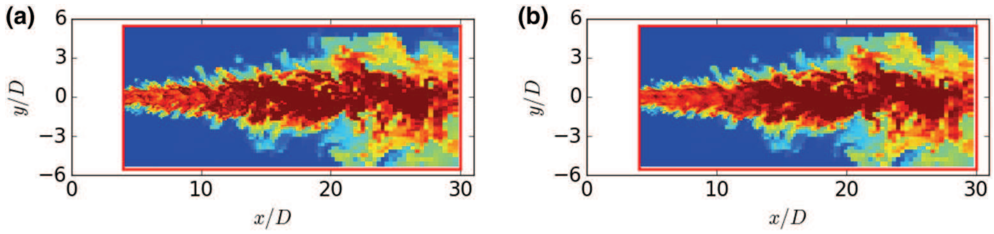

Fig. 7 Impact of temporal filter on a snapshot of temperature ($tU_J/D = 300$): **a** $f_{\text{filt}} = f_{\text{Nyq}}$, and **b** $f_{\text{filt}} = 0.4 f_{\text{Nyq}}$

normalization of different variables and the reconstruction error. Second, the results corresponding to the POD of the velocity, temperature and pressure are presented (Sect. 4.2), and finally, the results corresponding to the same variables plus the mass fractions are addressed (Sect. 4.3).

4.1 POD algorithm

The application of POD in fluid mechanics was introduced by [36], and later established in its classical formulation [18]. A more recent and wider presentation of the POD fundamentals and its applications can be found, for example, in [3]. Despite the basic interest of the underlying continuous formulation, POD is always applied in practice to discrete data, and we have opted to stick to the discrete formulation. The value of the flow variable i at the spatial location (x, r, θ) and time instant t is $f_i(x, r, \theta, t)$. The cylindrical grid is formed of $N_x \times N_r \times N_\theta$ cells, and the flowfield is sampled at S time instants. The snapshots for the ith variable can be encapsulated in the data matrix:

$$X^i = \begin{pmatrix} f_i(x_1, r_1, \theta_1, t_1) & \dots & f_i(x_1, r_1, \theta_1, t_S) \\ . & \dots & . \\ f_i(x_{N_x}, r_{N_r}, \theta_{N_\theta}, t_1) & \dots & f_i(x_{N_x}, r_{N_r}, \theta_{N_\theta}, t_S) \end{pmatrix}.$$

Prior to performing POD, the temporal means of each individual row has been subtracted from the data matrices, leaving purely zero-mean rows in X^i. The ROM will be obtained solely for the unsteady component of the jet. A ROM for the complete jet (containing the mean flow) can be obtained *a posteriori* by adding back the temporal means.

If there exists a homogeneous direction for which the data are periodic, POD modes are equal to Fourier modes in that direction [3,37]. In such a case, it is better to first Fourier transform the data along the homogeneous direction prior to applying the spatial POD algorithm. This decouples the POD decomposition for the various Fourier modes. In a circular jet, the data in the azimuthal direction being periodic, we Fourier transform the snapshots in the θ direction:

$$f_{im}(x, r, t) = \sum_{n=0}^{N_\theta - 1} f_i(x, r, \theta_n, t) \exp(-\mathrm{j} m \theta_n), \quad -N_\theta/2 \le m \le N_\theta/2, \tag{1}$$

$$f_i(x, r, \theta_n, t) = \frac{1}{N_\theta} \sum_{m=-N_\theta/2}^{N_\theta/2} f_{im}(x, r, t) \exp(\mathrm{j} m \theta_n), \; 0 \le n < N_\theta. \tag{2}$$

Here, we have assumed that the number of points in the azimuthal direction N_θ is odd, so that: $N_\theta = 2(N_\theta/2) + 1$. The transformed flowfield can be encapsulated in the following (complex) data matrices:

$$X^i_m = \begin{pmatrix} f_{im}(x_1, r_1, t_1) & \dots & f_{im}(x_1, r_1, t_S) \\ . & \dots & . \\ f_{im}(x_{N_x}, r_{N_r}, t_1) & \dots & f_{im}(x_{N_x}, r_{N_r}, t_S) \end{pmatrix}.$$

The size of these matrices is $Nx \times Nr \times S$. The snapshots for a series of R variables $i = 1 \cdots R$ can be gathered as:

$$X = \begin{pmatrix} X^1 \\ \vdots \\ X^R \end{pmatrix} \text{ and } X_m = \begin{pmatrix} X^1_m \\ \vdots \\ X^R_m \end{pmatrix}.$$

The standard version of POD (as opposed to spectral POD) is used here, in which the temporal homogeneity of the flow is ignored. In this case, POD is equivalent to the singular value decomposition of X_m:

$$X_m = U_m \Sigma_m V_m^*. \tag{3}$$

The left singular vectors forming U_m are the spatial POD modes, or topos (eigenvectors of the matrix $X_m X_m^*$), while the right singular vectors forming V_m are the temporal POD modes, or chronos (eigenvectors of the matrix $X_m^* X_m$). The singular values are the square roots of the energies of the POD modes, which are re-ordered so that $\sigma_{m1} > \sigma_{m2} > \cdots > \sigma_{mS} > 0$. The original data matrices X_m are *exactly* reconstructed using the S POD modes. Optimum N-rank approximations of the data matrix are directly obtained from Eq. (3) restricting to the leading N POD modes:

$$X_m \approx X_{mN} = U_{mN} \Sigma_{mN} V_{mN}^*, \tag{4}$$

where U_{mN} and V_{mN} are obtained by retaining only the N leading columns of U_m and V_m, and Σ_{mN} is the upper-left (N, N) block of Σ_m.

The original data matrix being real, its Fourier spectrum along θ obeys the complex conjugate symmetry: $X_{-m} = X_m^*$ for all m, which in turn implies that X_0 is real. The topos and chronos of X_m obey also this symmetry: $U_{-mn} = U_{mn}^*$, $V_{-mn} = V_{mn}^*$ for all m, n; and the energies fulfill: $\sigma_{-mn} = \sigma_{mn}$, for all m, n. The total energy is then equal to:

$$E = ||X||_F^2 = \langle X, X\rangle_F = \sum_{m=-N_\theta/2}^{N_\theta/2} \sum_{n=1}^{S} \sigma_{mn}^2 = \sum_{n=1}^{S} \sigma_{0n}^2 + 2 \sum_{m=1}^{N_\theta/2} \sum_{n=1}^{S} \sigma_{mn}^2, \tag{5}$$

where $\langle A, B\rangle_F = \mathrm{trace}(A^* B)$ is the Fröbenius inner product of a matrix and $|| \cdot ||_F$ its derived norm. The energies are normalized by the total energy to obtain the energy fractions. These are then expressed as a one-sided spectrum ($m \geq 0$):

$$\frac{\sigma_{0n}^2}{E} \text{ for } m = 0, \text{ and } \frac{2\sigma_{mn}^2}{E} \text{ for } m > 0. \tag{6}$$

Summing over all azimuthal modes, the energy fraction of the nth POD mode is: $\sigma_{0n}^2/E + 2\sum_{m=1}^{N_\theta/2} \sigma_{mn}^2/E$. Summing over all POD modes, the energy fraction associated to the mth azimuthal mode is: $\sum_{n=1}^{S} \sigma_{0n}^2/E$ for $m = 0$, and $2\sum_{n=1}^{S} \sigma_{mn}^2/E$ for $m > 0$.

4.1.1 Scalar product

A weight matrix, Q, can easily be introduced in the formulation. The data matrix X_m is replaced by $\underline{X}_m = Q^{1/2} X_m$, and U_m is replaced by $\underline{U}_m = Q^{1/2} U_m$:

$$X_m^* Q X_m = \underline{X}_m^* \underline{X}_m, \tag{7}$$

$$\underline{U}_m = \underline{X}_m \underline{V}_m \underline{\Sigma}_m^{-1}, \tag{8}$$

$$\underline{X}_m = \underline{U}_m \underline{\Sigma}_m \underline{V}_m^*, \tag{9}$$

$$\underline{X}_m \approx \underline{X}_{mN} = \underline{U}_{mN} \underline{\Sigma}_{mN} \underline{V}_{mN}^*. \tag{10}$$

The topos and the reconstructed data matrix corresponding to physical space can be recovered by re-scaling back:

$$U_m = Q^{-1/2} \underline{U}_m, \, X_{mN} = Q^{-1/2} \underline{X}_{mN}. \tag{11}$$

The weight matrix Q acts as a spatial scalar product. In order to transform back to physical space, Q needs to be regular. As any (real) scalar product, it needs to be symmetric and positive-definite. In the present study, Q is always diagonal, with the diagonal elements being set equal to the corresponding grid cell volumes, in order to account for the non-uniform grid cell size. All topos and reconstructed snapshots shown along the manuscript correspond to physical space.

4.1.2 Global products between variables

The amount of similarity between two variables i and j, averaged over all time instants, may be quantified through the normalized Fröbenius inner product:

$$C^{ij} = \frac{\langle \underline{X}^i, \underline{X}^j \rangle_F}{||\underline{X}^i||_F ||\underline{X}^j||_F}. \tag{12}$$

By definition, $C^{ii} = 1$, and $-1 \leq C^{ij} \leq 1$, i.e., 0 referring to orthogonal variables, and ± 1 to variables proportional to each other. In the following, the normalized Fröbenius inner product is called global product, for simplicity.

Equivalent expressions for the global products of individual azimuthal modes can be obtained by considering the matrices $\underline{X}_m^i$ instead of $\underline{X}^i$.

4.1.3 Normalization of dimensionally independent variables

In the special case of incompressible flow, the only dynamically independent variables are the velocity components, which have units of square root of energy per unit mass. In this case, the POD scalar product is said to be energy-based. For isentropic compressible flow, it is also possible to use an energy-based scalar product by using the square root of the stagnation internal energy (or enthalpy) as an additional variable [6], expressed in terms of the speed of sound a: $\sqrt{2\alpha/(\gamma-1)}a$ ($\alpha = 1$ for the internal energy, and $\alpha = \gamma$ for the enthalpy). But the reacting supersonic jet considered in this study is far from isentropic. Also, we wish to include variables in the POD analysis with different physical units. A way around this problem was proposed by Poje and Lumley [38], which consists in normalizing each variable by a constant parameter, prior to forming the auto-correlation matrices, so that the average projection of the normalized data matrix of each variable on its topos is the same for all variables. They showed that this condition is approximately fulfilled when the normalizing parameters are equal to the standard deviations of each variable. Hence, the normalizing parameter of variable i is:

$$K_i = ||\underline{X}^i||_F = \sqrt{\mathrm{trace}((X^i)^* \hat{Q}^i X^i)}, \tag{13}$$

which is computed and applied prior to the Fourier transform along θ. This normalization ensures that all variables have equal weight in the POD. In order to retain the relative amplitudes between the three components of the velocity, they have been assigned a single normalizing parameter: $K_{u,v,w} = \sqrt{||\underline{X}^u||_F^2 + ||\underline{X}^v||_F^2 + ||\underline{X}^w||_F^2}$.

4.1.4 Reconstruction error

When N POD modes are retained, the error of the reconstructed flowfield, or POD truncation error, corresponding to the azimuthal mode m is:

$$\mathrm{error}_{\mathrm{POD},m} = \frac{||\underline{X}_m - \underline{X}_{mN}||_F^2}{||\underline{X}_m||_F^2} = \frac{\sum_{n=N+1}^{S} \underline{\sigma}_{mn}^2}{\sum_{n=1}^{S} \underline{\sigma}_{mn}^2}. \tag{14}$$

Retaining M azimuthal modes, the global POD truncation error is:

$$\mathrm{error}_{\mathrm{POD}} = \frac{\sum_{M<|m|<N_\theta/2} \sum_{n=N+1}^{S} \underline{\sigma}_{mn}^2}{\sum_{m=-N_\theta/2}^{N_\theta/2} \sum_{n=1}^{S} \underline{\sigma}_{mn}^2}. \tag{15}$$

The cumulative energy fraction of the reconstructed flowfield is equal to $1 - \mathrm{error}_{\mathrm{POD}}$.

Note that the truncation error of any single flow variable i needs to be computed directly from the definition:

$$\mathrm{error}^i_{\mathrm{POD},m} = \frac{||\underline{X}_m^i - \underline{X}_{mN}^i||_F}{||\underline{X}_m^i||_F} \tag{16}$$

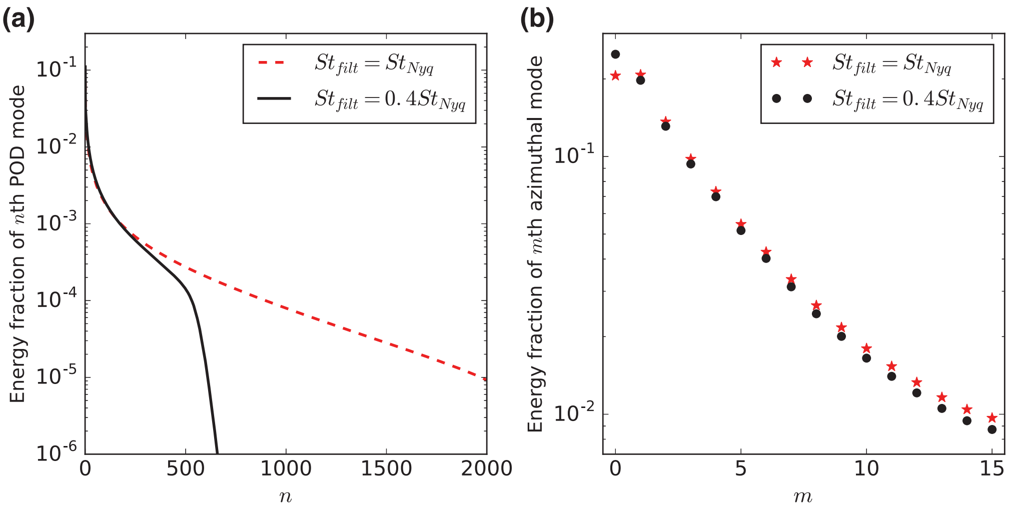

Fig. 8 **a** Effect of the low-pass filter on the energy fractions of the POD modes for the sum of all azimuthal modes, and **b** effect on the energy fractions of the azimuthal modes, for the sum of all POD modes

4.2 Results for POD(u, v, w, T, P)

In the first place, we consider a POD based on the temperature, the pressure and the three velocity components. The mass fractions of the species involved in the computation of the infrared radiation will be incorporated in Sect. 4.3.

The dataset used contains 2078 snapshots taken at a sampling rate $\mathrm{St_{samp}} = 1.12$ (see Sect. 3.2.1), and the simulation time is $1750 D/U_J$. If not stated otherwise, the cutoff frequency of the low-pass filter has been set to $\mathrm{St_{filt}} = 0.4\mathrm{St_{Nyq}} = 0.2\mathrm{St_{samp}}$ (see Sect. 3.2.2).

The procedure is as described in Sect. 4: (1) normalization of the data matrices of the flow variables (Sect. 4.1.3), (2) Fourier transform along θ and (3) POD for each azimuthal wavenumber. Scalar product matrices Q and $\hat{Q}$ are used to account for the non-uniform cell size (Sect. 4.1.1).

4.2.1 Energy decay

First, the impact of the low-pass filter on the POD is assessed. The energy fraction of the POD modes for the entire set of azimuthal modes is shown in Fig. 8a, with and without the low-pass filter. It is remarked that the normalization of the variables is applied after the low-pass filter, so that the total energy is the same whether the filter is applied or not. The effect of the low-pass filter is clear: it causes an decrease of the energy fractions of the high-order POD modes, while slightly increasing the energy fractions of the low-order POD modes (the latter is difficult to appreciate due to the log scale). The result is the focusing of the energy on the low-order modes, i.e., an increase of self-coherence. A sharp cutoff is observed at $n \approx 500$, suggesting that the POD modes $n > 500$ are associated to frequencies higher than the filter cutoff. This is, however, not accurate, as the POD modes contain in general a range of frequencies. The filter also removes the small frequency component of the low-order modes and moves to the low-order modes the low-frequency content that existed in the high-order modes. Figure 8b shows the energy fractions of the azimuthal modes (with all POD modes retained). The low-pass filter diminishes the energy of the modes $m > 1$ more than $m = 0$. The result is an increase of the energy fraction of $m = 0$ and a decrease of the energy fractions of the modes $m > 1$. As opposed to the energy distribution of the POD modes, no cutoff is observed.

Figure 9a, b shows the energy fractions (with the low-pass filter) of the individual POD modes as a function of n and m, respectively. The leading POD mode of $m = 0$ is, by far, the most energetic mode. Overall, the $m = 0$ and $m = 1$ azimuthal modes have similar energies and dominate the higher-order azimuthal modes. Like the POD modes, azimuthal modes of increasing order have decreasing energies. It is observed that the energies of the 2nd and the 3rd POD modes corresponding to $m = 0$ are close to each other. This is a sign of so-called mode pairing, i.e., two POD modes describing the same flow structure, convected downstream [37,39,40]. In general, for purely convecting flow structures the POD modes become Fourier modes, exhibiting a complex structure (real and imaginary components). This mode pairing phenomenon exists only for real POD

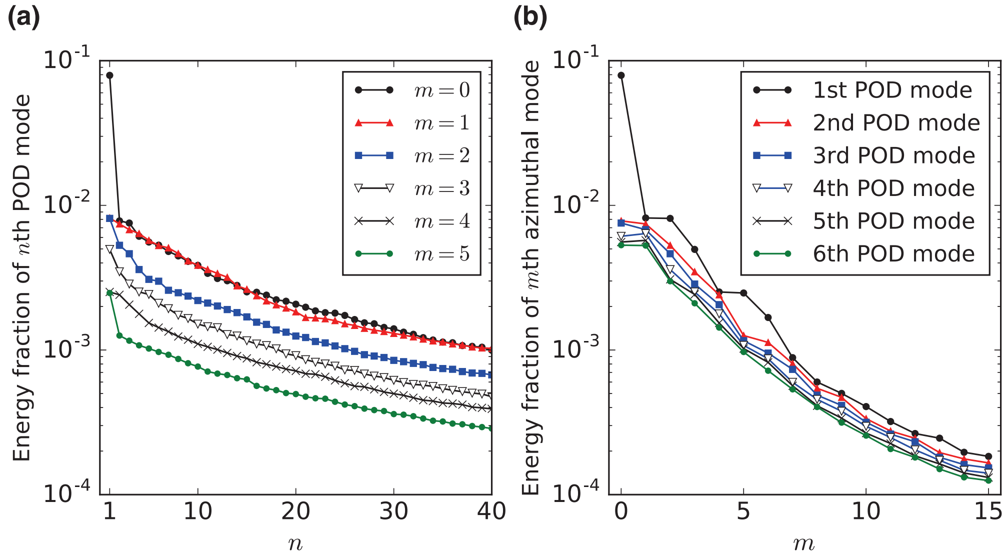

Fig. 9 **a** Energy fractions of the POD modes for a given azimuthal mode and **b** energy fractions of the azimuthal modes, for a given POD mode. $m = 0$ modes number 2 and 3 are paired and are associated to a compressible axisymmetric shear layer instability. Paired modes exist only for $m = 0$, as POD modes for $m \neq 0$ are complex

Table 1 Cumulative energy fraction for the leading N POD modes and the leading M azimuthal modes, with and without the low-pass filter ($\mathrm{St_{filt}} = 0.4\mathrm{St_{Nyq}}$)

	$N = 1$		$N = 10$		$N = 100$		$N = 200$	
	No filter (%)	Filter (%)	No filter (%)	Filter (%)	No filter (%)	Filter (%)	No filter (%)	Filter (%)
$m = 0$ ($M = 1$)	4.2	7.9	7.9	13.2	15.3	21.5	17.3	23.2
$m = 0, \ldots, 4$ ($M = 5$)	6.2	10.3	19.4	27.7	46.4	57.5	55.0	65.9
$m = 0, \ldots, 9$ ($M = 10$)	6.8	10.9	22.4	31.3	55.9	68.7	67.1	79.7

modes ($m = 0$ in this case). Further evidence that these two POD modes are paired comes from their spatial and temporal structure, which will be analyzed in Sect. 4.2.3.

Table 1 shows the cumulative energy fraction of the reconstructed flowfield, with and without the low-pass filter. For each of the leading M azimuthal modes, the N leading POD modes are retained, so that the flowfield is reconstructed using $N \times M$ POD modes. Without the filter, the leading 10 POD modes and 10 azimuthal modes account for 22% of the total energy, while they contain 31% of the energy with the filter. Even using the low-pass filter, the limited energy fraction associated to the leading POD mode of the 10 leading azimuthal modes is appreciated. It contains a mere 11% of the energy. This value has been shown to be higher for lower Reynolds number jets [2,19], or when POD is applied to smaller sets of uncorrelated snapshots or coarser spatial grids [1], or for smaller sets of variables and smaller regions [1,2,4].

The flowfield of a given azimuthal mode can be approximately reconstructed using a reduced number of POD modes. The snapshots reconstruction helps visualizing the impact of the POD truncation. Figures 10 and 11 show the $m = 0$ component of an axial velocity snapshot and a temperature snapshot, respectively (a), together with the reconstruction using $N = 80$ POD modes (b). The reconstructed snapshots corresponding to the full spatiotemporal reduction (c) will be discussed in Sect. 5.4. The reconstructed snapshots using 80 POD modes mimic well the largest structures, while damping the local, high intensity peaks and the low-energy, small-scale structures.

4.2.2 Energy distribution in frequency

It has been observed in the previous subsection that a low-pass frequency filter diminishes drastically the energy of the modes above a certain order, while the lower order modes remain approximately unaffected. The explanation can be found looking at the frequency spectrum of the chronos. In Fig. 12a, b, time samples and the corresponding frequency spectra of the 1st, 8th and 24th $m = 1$ chronos are shown. Higher-order modes

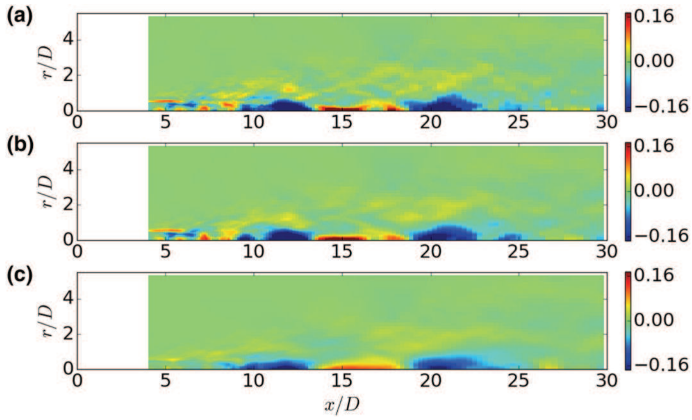

Fig. 10 **a** Axisymmetric $m = 0$ component of axial velocity snapshot (taken at $1500D/U_J$, after the low-pass filter), **b** reconstruction corresponding to the spatial reduction with $N = 80$ POD modes, and **c** reconstruction corresponding to the spatiotemporal reduction with $N = 80$ POD modes and $F = 80$ Fourier modes (all normalized by the reference velocity, U_J)

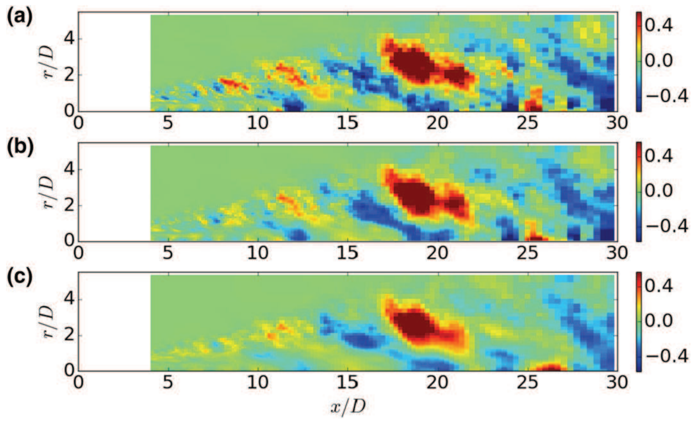

Fig. 11 **a** Axisymmetric $m = 0$ component of temperature snapshot (taken at $1500D/U_J$, after the low-pass filter), **b** reconstruction corresponding to the spatial reduction with $N = 80$ POD modes, and **c** reconstruction corresponding to the spatiotemporal reduction with $N = 80$ POD modes and $F = 80$ Fourier modes (all normalized by the reference temperature, T_J)

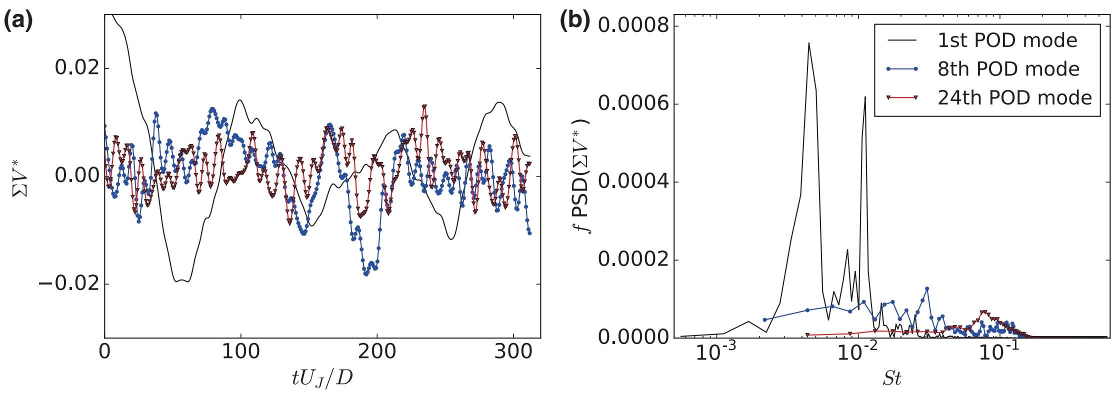

Fig. 12 Frequency content of $m = 1$ leading chronos: **a** real component in time and **b** PSD of the 1st, 8th and 24th chronos

display higher spectral levels at higher frequencies. This is observed for all azimuthal modes. This behavior reveals a spatiotemporal hierarchy present in all turbulent flows. The large scales associated to low-frequency motions are the most energetic, and the power spectrum decays at higher frequencies, which are associated to smaller scales. Thus, the low-pass frequency filter and the POD truncation (effectively a low-pass energy filter) both induce a low-pass filtering in space.

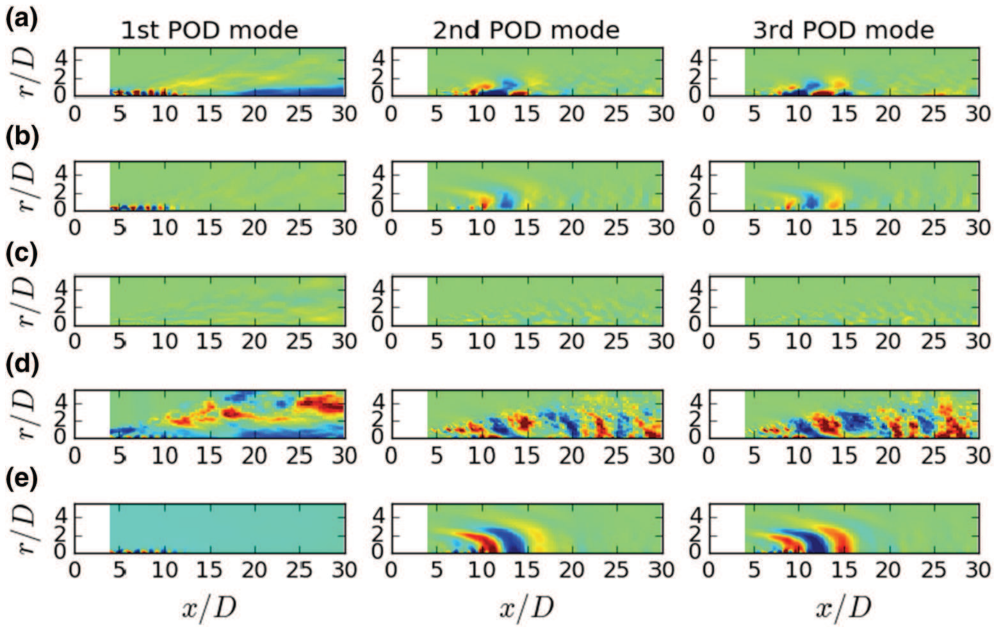

Fig. 13 Colormaps of the 3 leading $m = 0$ topos of **a** the axial velocity, **b** radial velocity, **c** azimuthal velocity, **d** temperature and **e** pressure

4.2.3 Dominant POD modes

Figure 13a–e shows respectively the 3 leading $m = 0$ topos of the axial, radial, azimuthal velocity, temperature and pressure. Figure 14a–e refers to the same data but for $m = 1$. In order to fully appreciate their features, the colormaps are normalized by 60% of their respective maximum and minimum values (with the exception of the three velocity components, whose colormaps are equal for a given POD mode). Their energies (Fig. 9) are a measure of their actual relative amplitudes. The spectra of the corresponding chronos are plotted in Fig. 15a ($m = 0$) and b ($m = 1$). As can be appreciated, the amplitude of the $m = 0$ azimuthal velocity component is much weaker than the other velocity components and should be interpreted as noise.

The leading topos of $m = 0$ of the axial / radial velocity components, as well as the pressure, peak sharply on the shock cells, within the potential core. The temperature peaks also in that region, but shows as well a high amplitude, large-scale perturbation well downstream. This mode appears as an intense pulsating motion linked to the shock cells and has a very low frequency, as observed in Fig. 15a (the spectrum peaks at $\mathrm{St} \approx 0.0006$, the minimum resolved frequency). Much longer acquisition times would be needed to accurately estimate this frequency. Its associated acoustic wavelength is about $200D$, much larger than the region of the ROM. A possible interpretation of this mode is a compression wave interacting intensely with the shock cells, which appears as a non-traveling mode due to its wavelength being much larger than the POD region. The 2nd and 3rd topos are similar and appear to be phase-shifted in the axial direction. This suggests that they are actually paired. Their amplitude grows until the end of the potential core, before decaying downstream (with the exception of the temperature). The topos of the temperature are more irregular and do not decay downstream. The PSD of the 2nd and 3rd chronos are nearly identical and peak at $\mathrm{St} = 0.05$. The relative phase between the 2nd and 3rd topos (arc tangent of the 3rd topos divided by the 2nd topos) along the jet lip line is shown in Fig. 16, and the relative phase between the 2nd and 3rd chronos (minus the arc tangent of the 3rd chronos divided by the 2nd chronos) in Fig. 17. The slope of the relative phase of the topos is a local (in space) measure of the axial wavenumber of the structure. All variables clearly show a unique wavenumber within $10D < x < 16D$. Downstream, the wavenumber of the velocities and the temperature diminish, while the wavenumber of the pressure roughly remains constant. The slope of the relative phase between the 2nd and 3rd chronos is a local (in time) measure of the frequency of the structure. The phase increases monotonically at a roughly constant rate, indicating a well-defined global frequency. Together, a wavelength varying slowly in space and a frequency varying slowly in time establish the wave packet nature of this pair of POD modes. Wave packets are convected structures linked to linear convective instabilities of the mixing layer (the Kelvin–Helmholtz instability in subsonic jets [41,42], while other types of instabilities are also possible in supersonic

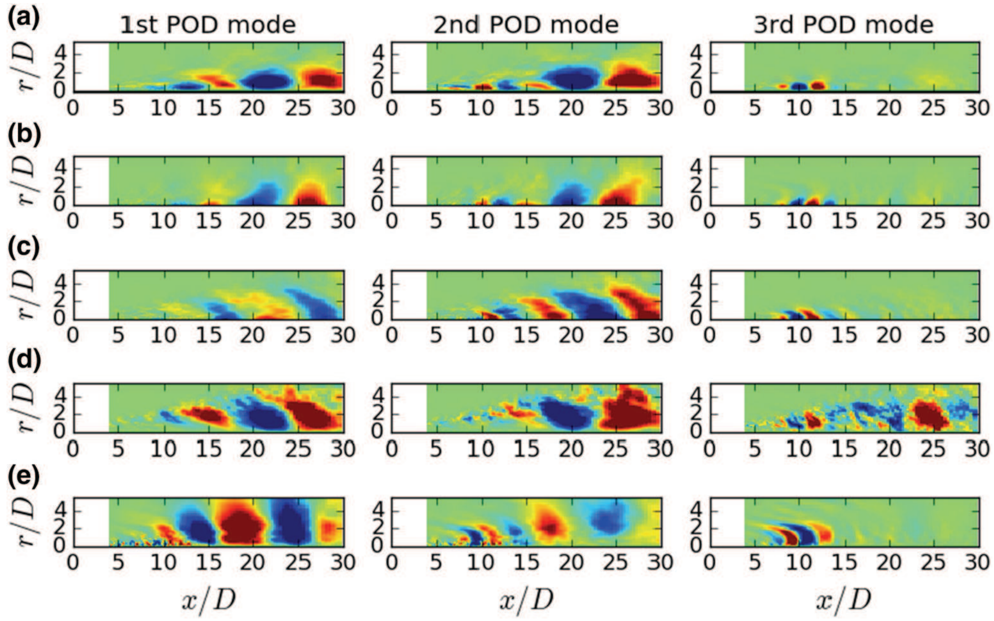

Fig. 14 Colormaps of the real component of the 3 leading $m = 1$ topos of **a** the axial velocity, **b** radial velocity, **c** azimuthal velocity, **d** temperature and **e** pressure

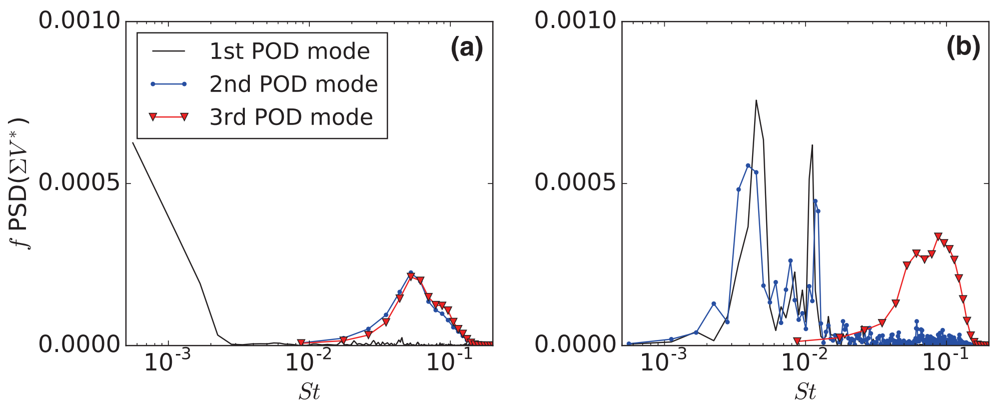

Fig. 15 PSD of the 3 leading chronos (weighed with the singular values) corresponding to **a** $m = 0$ and **b** $m = 1$

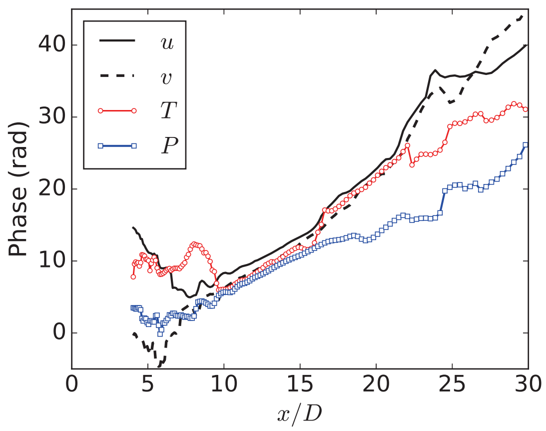

Fig. 16 Phase between the 2nd and 3rd $m = 0$ topos, along the lip line ($r = D/2$)

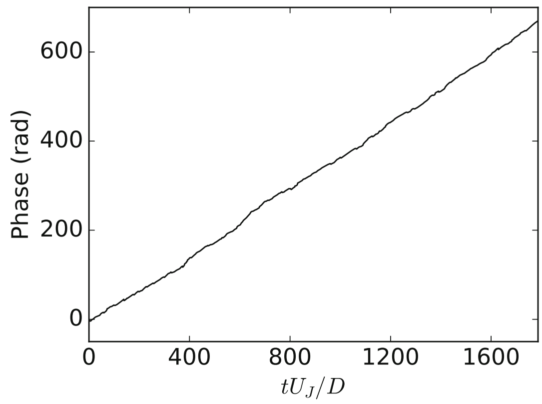

Fig. 17 Phase between the 2nd and 3rd $m = 0$ chronos

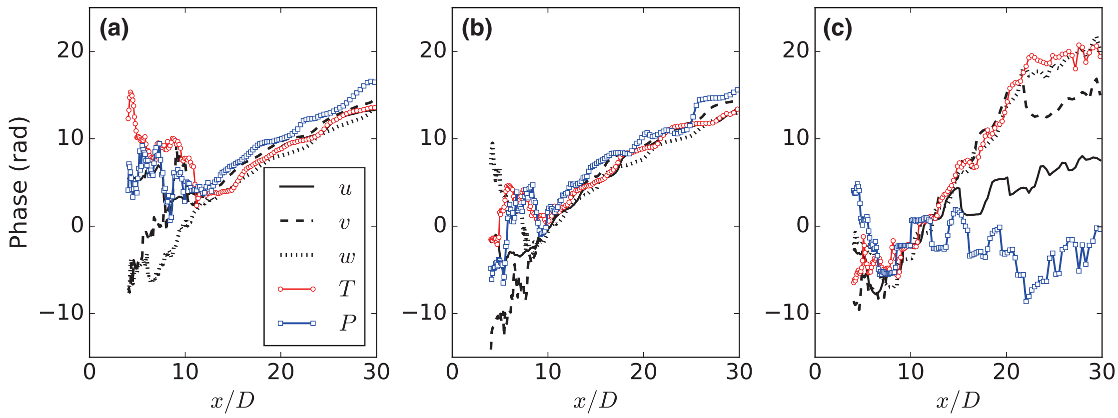

Fig. 18 Phase of the **a** 1st, **b** 2nd and **c** 3rd $m = 1$ topos, along the lip line ($r = D/2$)

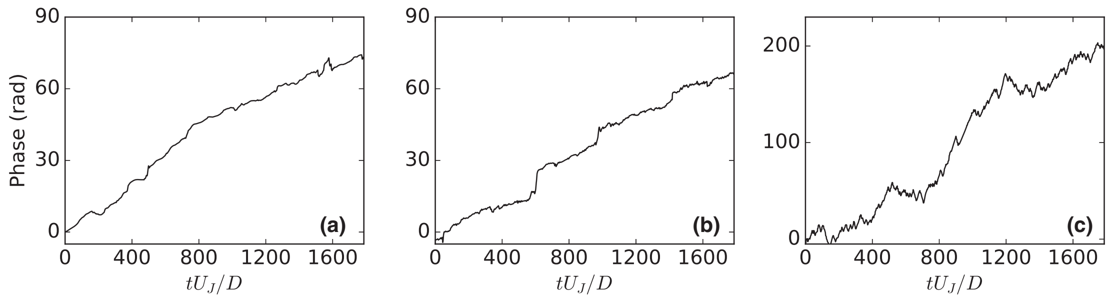

Fig. 19 Phase of the **a** 1st, **b** 2nd and **c** 3rd $m = 1$ chronos

jets [43–45]. The deviations of the temperature from the other variables can be explained by the existence of the flame, which strengthens when moving downstream. It is remarkable that the velocity and pressure characteristics of the wave packet remain largely unaffected by the strengthening of the flame.

The 1st and 2nd $m = 1$ topos peak downstream of the potential core and show no interaction with the shock cells. All variables reveal coherent structures approximately periodic along the jet axis, with a certain wavelength. The PSD of the 1st and 2nd chronos exhibit two common peaks at low frequencies: St ≈ 0.005 and St ≈ 0.01. They share two common spectral peaks, display similar wavelengths, but their energies are not particularly close to each other (see Fig. 9a). The phase (arc tangent of the imaginary component divided by the real component) of the 1st, 2nd and 3rd topos along the jet lip line is shown in Fig. 18a–c, respectively. The 1st and 2nd POD modes exhibit similar axial wavenumbers for $x > 10D$, before progressively diminishing downstream, indicating a growth of the spatial structures. The phase (arc tangent of the imaginary and real parts) of the 1st, 2nd and 3rd chronos is shown in Fig. 19a–c, respectively. The phase of the 1st chronos

Table 2 Centerline velocity along the jet (U_0/U_J), Strouhal number based on the centerline velocity (fD/U_0) associated to the peak at $fD/U_J = 0.01$ of the 1st and 2nd POD modes of $m = 1$, and associated convection-to-centerline velocity ratio ($U_c/U_0 = \lambda f/U_0$)

	$x = 5D$	$x = 10D$	$x = 15D$	$x = 20D$
U_0/U_J	0.7	0.56	0.31	0.21
fD/U_0	0.014	0.018	0.032	0.048
U_c/U_0	0.171	0.214	0.387	0.571

increases linearly before undergoing a slope change, at about $800D/U_J$, and then again shows a linear growth at a somewhat lower rate until the end of the time sequence. This can be explained by the similarity of the 1st and 2nd POD modes, which obviously represent a mix of two different wave packets. The lowest frequency peak in the PSD of the chronos and the lowest phase growth rate observed in the chronos are associated to one wave packet, while the highest frequency peak and the high phase growth rate portion of the chronos are associated to another wave packet with a faster convection velocity. Since the jet shear layer thickens progressively downstream, it is possible that these low-frequency wave packets are associated to a shear layer instability of the jet. This instability is characterized by a convection velocity of about half the jet centerline velocity. The convection velocity at their two spectral peaks is estimated as the wavelength times the frequency: $U_c/U_J = \lambda \mathrm{St}/D \approx 0.06$ and 0.12. Table 2 shows the Strouhal number and the convection velocity normalized with the jet centerline velocity, at various distances from the nozzle exit. The convection-to-centerline velocity ratio increases downstream, reaching a value of 0.29 (1st peak) and 0.57 (2nd peak) at $x = 20D$. Therefore, based on their convection velocity, the 1st and 2nd POD modes could be associated to a Kelvin–Helmholtz instability in the subsonic downstream region. The 3rd POD mode is different from the previous ones. It reveals a coherent structure roughly periodic downstream, but it peaks by the end of the potential core and displays a smaller wavelength. The PSD of its chronos is broadband and peaks at $\mathrm{St} \approx 0.1$. The phase of the 3rd topos along the jet lip line reveals differences between the variables. An axial wavenumber can be globally inferred from the velocity components and the temperature, but not from the pressure, which has a more irregular pattern. A phase growth rate can be also deduced from the 3rd chronos, at least globally. The evidence points also to an approximate wave packet structure of the 3rd POD mode.

In spectral POD (where POD is performed in the frequency domain [4,46]), it is easier to identify linear wave packets because POD modes are restricted to a single frequency (the chronos have the form $\exp(j2\pi ft)$). This is not the case in the present standard form of POD, where the chronos are only freely evolving unitary orthogonal vectors. Yet, wave packet-like structures can still be identified as long as the phase slope along the x-axis of the topos and the phase slope of the chronos vary slowly, defining a local (in space) axial wavelength and a local (in time) frequency, respectively. In order to filter linear wave packets (solutions to the linearized equations), spectral POD is required in order to prevent the mixing of modes of similar energies.

Several of the leading topos reveal a change in spatial pattern downstream of a certain axial position (see the 2nd topos of $m = 1$ in Fig. 14). In particular, they show an increase in both axial wavelength and radial size there. A discontinuity in the wave packet structures was also observed by Schmidt et al. [45] in both the spectral POD modes and the sub-optimal resolvent modes. They concluded those modes are actually composed of multiple linear modes that are similarly amplified, through the Orr mechanism. It is a possibility that the mixed modes found in the present jet are a manifestation of this mechanism. However, given that the present POD modes contain multiple frequencies, it is likely that the spatial discontinuities observed here result from the mixing of modes with similar energy and different frequencies, instead of linear sub-optimal modes.

4.3 POD(u, v, w, T, P, Y_{OH}, Y_{CO2}, Y_{H2O}, Y_{CO})

In this section, the mass fractions of a number of chemical species are added in the POD analysis. The application of interest for the ROM in this case is the computation of the infrared radiation emitted by the jet. The flow variables needed to compute the radiated field are [20]: T, P, Y_{CO2}, Y_{H2O}, Y_{CO}.

The number of snapshots, sampling rate and simulation time is the same as in Sect. 4.2. Also, the low-pass filter is applied prior to POD, with a cutoff frequency of $\mathrm{St}_{\mathrm{filt}} = 0.4\mathrm{St}_{\mathrm{Nyq}} = 0.2\mathrm{St}_{\mathrm{samp}}$.

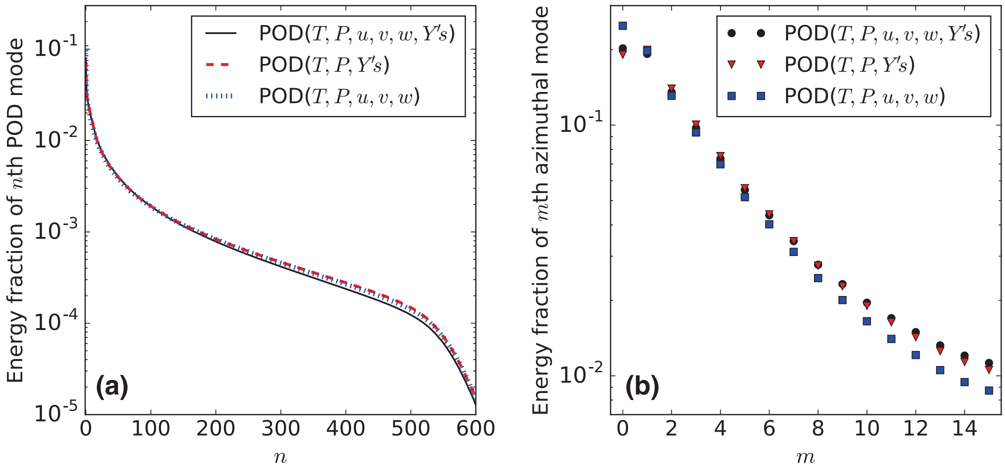

Fig. 20 Energy fractions corresponding to POD(T, P, u, v, w), POD(T, P, Y_{CO2}, Y_{H2O}, Y_{CO}) and POD(T, P, u, v, w, Y_{OH}, Y_{CO2}, Y_{H2O}, Y_{CO}), for the sum of **a** all azimuthal modes and **b** the sum of all POD modes

4.3.1 Energy decay

The energy fractions of the POD modes corresponding to the set of variables needed to compute the infrared radiation (temperature, pressure, mass fractions of CO2, H2O and CO), as well as the former set plus the three velocity components and the mass fraction of OH, are shown in Fig. 20a, for the sum of all azimuthal modes. Figure 20b shows the energy fractions decomposed by azimuthal modes (sum of all POD modes). Adding the mass fractions to the scalar product has only a very weak impact on the decay rate of the energies. This indicates that the mass fractions do not add new energetically relevant spatial structures with respect to the reduced set of variables. There is however an impact on the energies of the azimuthal modes. Adding the mass fractions diminishes the energy fraction of the $m = 0$ mode and increases slightly the energy fractions of the remaining azimuthal modes. The variable that mostly contributes to $m = 0$ is the pressure, due to its intense interaction with the shock cells. The decrease in energy fraction of the $m = 0$ component when adding the mass fractions can thus be explained by the smaller relative weight of the pressure in the decomposition.

The energy decay rate for the set of variables that determine the infrared signature is close to the case with the entire set of variables. Therefore, no significant reduction (in relative terms) is obtained when focusing the reduction solely on the temperature, pressure and mass fractions of CO2, H2O and CO. In the rest of this section, we focus on the results pertaining to the scalar product involving all variables (velocities, temperature, pressure and mass fractions).

4.3.2 Dominant POD modes

Looking at the spatial structure of the leading topos (Figs. 21, 22), it is appreciated that the 1st topos for the axial velocity and temperature (a, b) resemble the 1st topos corresponding to the reduced set of variables, analyzed in the previous section (Fig. 13a, d), for $m = 0$. The frequency spectra of the chronos for the extended set of variables are shown in Fig. 23. Like the topos, the leading chronos of $m = 0$ is analogous to the previous case. The 3rd topos of $m = 0$ is similar to the previous 2nd and 3rd topos of $m = 0$, and so are the corresponding chronos spectra. The 3rd topos of $m = 0$ is actually paired to the 4th POD mode (not shown), and both describe a convected structure similar to a wave packet. The 2nd topos and chronos of $m = 0$, on the other hand, do not match any of the three leading POD modes for the reduced set of variables. This POD mode is not paired and, differently to the 1st POD mode, its wavelength is contained within the POD region. If it were a traveling mode it would be described by two POD modes. The interpretation of this POD mode is not clear. Strong parallelisms are also observed for $m = 1$. The 1st and 2nd topos and chronos are analogous to the case with the reduced set of variables and represent the same convecting flow structures. It is concluded that while some of the leading POD modes are very similar between the reduced and extended sets of variables, they are not the same in general, and their ordering can change.

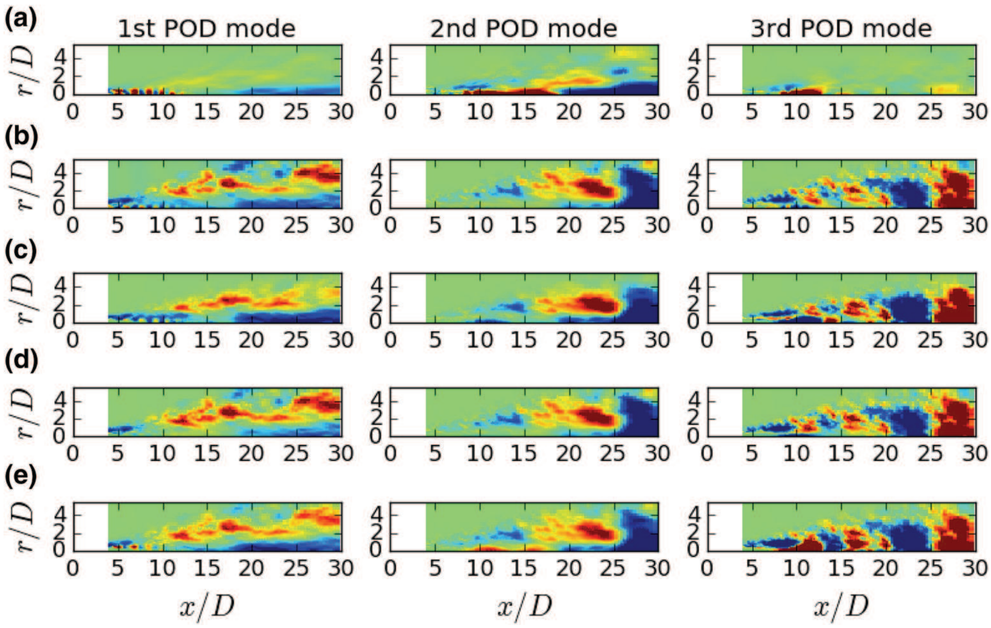

Fig. 21 Colormaps of the real part of the 3 leading $m = 0$ topos corresponding to **a** axial velocity, **b** temperature, **c** Y_{OH}, **d** Y_{CO2} and **e** Y_{H2O}

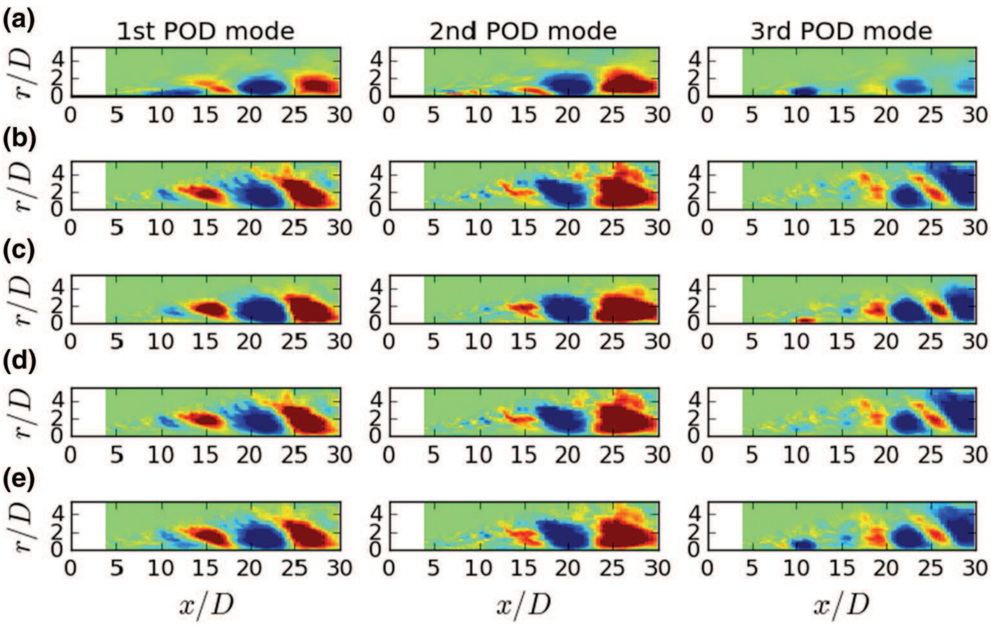

Fig. 22 Colormaps of the real part of the 3 leading $m = 1$ topos corresponding to **a** axial velocity, **b** temperature, **c** Y_{OH}, **d** Y_{CO2} and **e** Y_{H2O}

Turning now to the mass fractions, their mutual resemblance as well as their resemblance with the temperature can be appreciated, for both $m = 0$ and $m = 1$. Their relationship is further explored in the following from the global products.

4.3.3 Global affinity between variables

The global products (Eq. 12) of all variable pairs are shown in Table 3. The values $C^{ij} > 0.4$ and $0.4 > C^{ij} > 0.2$ are highlighted. A connection between the resemblance of the topos of the variable pairs (Figs. 21, 22) and

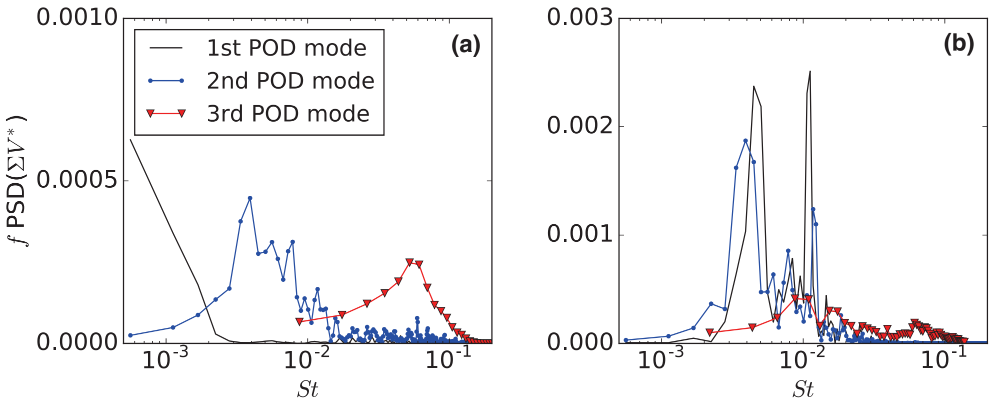

Fig. 23 Frequency spectrum of the 3 leading chronos of POD($u, v, w, T, P, Y_{OH}, Y_{CO2}, Y_{H2O}, Y_{CO}$), corresponding to **a** $m = 0$ and **b** $m = 1$

Table 3 Cross-products of all variable pairs. Strong similarity ($C^{ij} > 0.4$) is highlighted in bold, and moderate similarity ($0.2 < C^{ij} < 0.4$) is highlighted in italics

	u	v	w	T	P	Y_{OH}	Y_{CO_2}	Y_{H_2O}	Y_{CO}
Y_{CO}	*0.239*	*0.301*	0.009	**0.412**	− 0.065	**0.810**	**0.460**	**0.516**	1
Y_{H_2O}	*0.315*	**0.432**	− 0.004	**0.989**	− 0.118	**0.734**	**0.998**	1	
Y_{CO_2}	*0.310*	**0.427**	− 0.005	**0.994**	− 0.119	**0.706**	1		
Y_{OH}	*0.271*	*0.378*	0.009	**0.637**	− 0.085	1			
P	0.013	0.043	− 0.011	− 0.103	1				
T	*0.303*	**0.418**	− 0.007	1					
w	0.012	0.002	1						
v	**0.406**	1							
u	1								

the values in Table 3 can be drawn. The temperature has a high global product with all of the mass fractions, while the topos of the temperature and the mass fractions are remarkably similar. At the same time, the topos of the pairs of variables with a low global product are different. It appears that the global products dictate not only a global resemblance, but also the resemblance of the individual POD modes. This can be understood from the link between POD and the global products. Consider two variables, i and j. Their temporal auto-correlation matrix is:

$$\underline{X}^*\underline{X} = (\underline{X}^i)^*\underline{X}^i + (\underline{X}^j)^*\underline{X}^j. \tag{17}$$

If the variables have a global product approaching ± 1 implies they are approximately proportional to each other:

$$\underline{X}^j \approx k\underline{X}^i, \tag{18}$$

with k a constant scalar. In this case, the auto-correlation matrix becomes:

$$\underline{X}^*\underline{X} \approx (\underline{X}^i)^*\underline{X}^i + k^2(\underline{X}^i)^*\underline{X}^i = (1+k^2)(\underline{X}^i)^*\underline{X}^i = \left(1 + \frac{1}{k^2}\right)(\underline{X}^j)^*\underline{X}^j, \tag{19}$$

i.e., it is approximately proportional to the auto-correlation matrix of each variable individually. Therefore, in the case that the variables have a global product approaching ± 1, the POD modes corresponding to the pair of variables approach the POD modes of the individual variables, and explains why the topos are so similar. The high global products of the mass fractions with the temperature also explain the coincidence of the energy decay rates in Fig. 20a. Given their high global products, the temperature and the mass fractions Y_{CO2} and Y_{H2O} should be approximately proportional to each other. Figure 24 shows the time signals (with means removed) of the temperature and the mass fractions at a point downstream of the jet ($x = 20D$, $r = D/2$). The resemblance of T with Y_{CO2} and Y_{H2O} is remarkable and indeed suggests they are approximately proportional. Note that the proportionality constant, k, may need to change through space for a realistic fit. As long as its sign is the same everywhere, especially in the regions that contain most of the energy, the value of the global product is still guaranteed to be high. The link detected between the temperature and the mass fractions in the present jet could certainly be exploited in order to further reduce the flowfield.

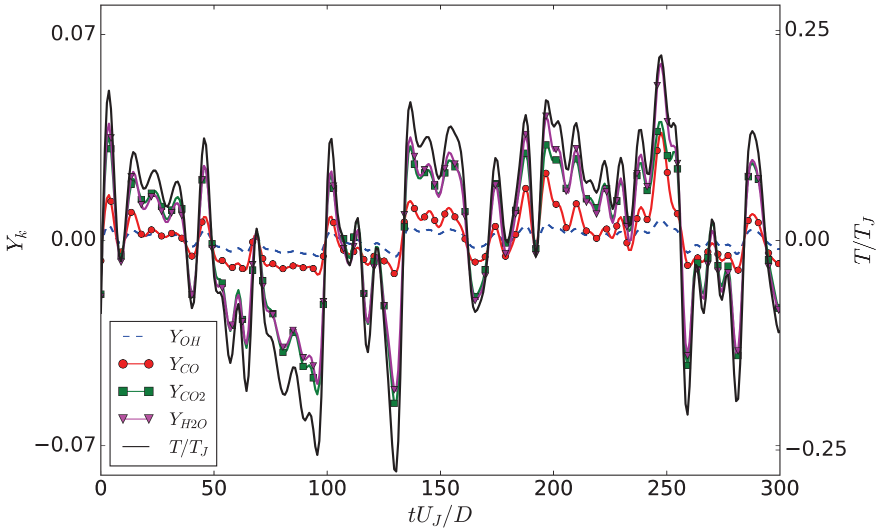

Fig. 24 Time signals of the temperature and the mass fractions (with means removed) at $x = 20D$, $r = D/2$

5 Temporal reduction

The approximate reconstruction of the mth azimuthal mode, using a POD basis of size N, is:

$$\underline{X}_m \approx \underline{X}_{mN} = \underline{U}_{mN}\underline{\Sigma}_{mN}\underline{V}^*_{mN} = \underline{U}_{mN}\Phi^*_{mN}, \tag{20}$$

where the matrix Φ_{mN} contains the temporal coefficients of the snapshots in the retained POD basis. Its dimension is $N \times S$, where S is the number of snapshots. The first goal of this section is to present and assess a temporal ROM for Φ_{mN}. Secondly, the full spatiotemporal ROM obtained from the POD truncation in Eq. (20) together with the temporal reduction will be assessed.

5.1 Reconstruction error

The performance of the temporal reduction has been quantified through the reconstruction error of Φ_{mN}:

$$\text{error}_{\Phi,m} = \frac{||\Phi_{mN} - \Phi_{mN,ROM}||_F^2}{||\Phi_{mN}||_F^2}. \tag{21}$$

The error of the spatial reduction is the POD truncation error:

$$\text{error}_{\text{POD},m} = \frac{||\underline{X}_m - \underline{U}_{mN}\Phi^*_{mN}||_F^2}{||\underline{X}_m||_F^2} = \frac{\sum_{n=N+1}^{S}\underline{\sigma}^2_{mn}}{\sum_{n=1}^{S}\underline{\sigma}^2_{mn}}. \tag{22}$$

And the error of the spatiotemporal ROM is:

$$\begin{aligned}
\text{error}_{ROM,m} &= \frac{||\underline{X}_m - \underline{U}_{mN}\Phi^*_{mN,ROM}||_F^2}{||\underline{X}_m||_F^2} = \frac{||\underline{X}_m - \underline{U}_{mN}\Phi^*_{mN} + \underline{U}_{mN}\Phi^*_{mN} - \underline{U}_{mN}\Phi^*_{mN,ROM}||_F^2}{||\underline{X}_m||_F^2} \\
&= \frac{||\underline{X}_m - \underline{U}_{mN}\Phi^*_{mN}||_F^2 + ||\Phi_{mN} - \Phi_{mN,ROM}||_F^2}{||\underline{X}_m||_F^2} \\
&\quad + \frac{\langle \underline{U}_m\Phi^*_m, \underline{U}_{mN}(\Phi_{mN} - \Phi_{mN,ROM})^*\rangle_F - \langle \underline{U}_{mN}\Phi^*_{mN}, \underline{U}_{mN}(\Phi_{mN} - \Phi_{mN,ROM})^*\rangle_F}{||\underline{X}_m||_F^2} \\
&\quad + \frac{\langle \underline{U}_{mN}(\Phi_{mN} - \Phi_{mN,ROM})^*, \underline{U}_m\Phi^*_m\rangle_F - \langle \underline{U}_{mN}(\Phi_{mN} - \Phi_{mN,ROM})^*, \underline{U}_{mN}\Phi^*_{mN}\rangle_F}{||\underline{X}_m||_F^2}
\end{aligned}$$

$$
\begin{aligned}
&= \frac{\sum_{n=N+1}^{S} \underline{\sigma}_{mn}^2 + ||\Phi_{mN} - \Phi_{mN,ROM}||_F^2}{\sum_{n=1}^{S} \underline{\sigma}_{mn}^2} + 0 + 0 \\
&= \frac{\sum_{n=N+1}^{S} \underline{\sigma}_{mn}^2}{\sum_{n=1}^{S} \underline{\sigma}_{mn}^2} + \frac{||\Phi_{mN} - \Phi_{mN,ROM}||_F^2}{||\Phi_{mN}||_F^2} \frac{||\Phi_{mN}||_F^2}{\sum_{n=1}^{S} \underline{\sigma}_{mn}^2} \\
&= \mathrm{error}_{\mathrm{POD},m} + \mathrm{error}_{\Phi,m} \frac{\sum_{n=1}^{N} \underline{\sigma}_{mn}^2}{\sum_{n=1}^{S} \underline{\sigma}_{mn}^2} \\
&= \mathrm{error}_{\mathrm{POD},m} + \mathrm{error}_{\Phi,m} (1 - \mathrm{error}_{\mathrm{POD},m}),
\end{aligned} \tag{23}
$$

where it has been used that $\underline{U}_{mN}^* \underline{U}_{mN} = I_N$, where I_N is the identity matrix, and that $\underline{X}_m^* \underline{U}_{mN} = \Phi \underline{U}_m^* \underline{U}_{mN} = \Phi_m (\frac{I_N}{0}) = \Phi_{mN}$. The matrices X_m, U_m, Φ_m correspond to the no-reduction case ($N = S$).

The error for the full spatiotemporal ROM using the M leading azimuthal modes is:

$$
\mathrm{error}_{\mathrm{ROM}} = \frac{\sum_{M \le |m| < N_\theta/2} \sum_{n=N+1}^{S} \underline{\sigma}_{mn}^2}{\sum_{m=-N_\theta/2}^{m=N_\theta/2} \sum_{n=1}^{S} \underline{\sigma}_{mn}^2} + \frac{\sum_{M \le |m| < N_\theta/2} ||\Phi_{mN} - \Phi_{mN,ROM}||_F^2}{\sum_{m=-N_\theta/2}^{m=N_\theta/2} \sum_{n=1}^{S} \underline{\sigma}_{mn}^2}. \tag{24}
$$

5.2 Fourier-based temporal ROM

We assume that the state of the system $\{\Phi_{mn}\}$ (column of Φ_{mN}) evolves in time according to:

$$
\frac{\mathrm{d}}{\mathrm{d}t} \{\Phi_{mn}\} = A_{F,m} \{\Phi_{mn}\}, \tag{25}
$$

where $A_{F,m}$ is a matrix of size $N \times N$ to be determined. The system is homogeneous because the temporal mean of the data in Φ_{mN} is zero. Applying a discrete Fourier transform to Φ_{mN}, we obtain the matrix $\hat{\Phi}_{mN}$, formed of S Fourier modes. A temporal reduction is imposed by retaining only F Fourier modes:

$$
\hat{\Phi}_{mN}^F = \Phi_{mN} \begin{pmatrix} \exp(-j2\pi f_1 t_1) & \ldots & \exp(-j2\pi f_F t_1) \\ \vdots & \ddots & \vdots \\ \exp(-j2\pi f_1 t_S) & \ldots & \exp(-j2\pi f_F t_S) \end{pmatrix} = \Phi_{mN} [\exp(-j2\pi f t)]^F. \tag{26}
$$

The matrix Φ_{mN} can then be approximately reconstructed from $\hat{\Phi}_{mN}^F$ using the inverse discrete Fourier transform:

$$
\Phi_{mN} \approx \frac{1}{F} \hat{\Phi}_{mN}^F \begin{pmatrix} \exp(j2\pi f_1 t_1) & \ldots & \exp(j2\pi f_1 t_S) \\ \vdots & \ddots & \vdots \\ \exp(j2\pi f_F t_1) & \ldots & \exp(j2\pi f_F t_S) \end{pmatrix} = \frac{1}{F} \hat{\Phi}_{mN}^F ([\exp(-j2\pi f t)]^F)^*. \tag{27}
$$

Considering now a continuous time t, the time derivative of Eq. (27) is approximated as

$$
\frac{\mathrm{d}}{\mathrm{d}t} \Phi_{mN} \approx \frac{1}{F} \hat{\Phi}_{mN}^F \begin{pmatrix} j2\pi f_1 & 0 & 0 \\ 0 & \ddots & 0 \\ 0 & 0 & j2\pi f_F \end{pmatrix} ([\exp(-j2\pi f t)]^F)^* = \frac{1}{F} \hat{\Phi}_{mN}^F [j2\pi f]^F ([\exp(-j2\pi f t)]^F)^*, \tag{28}
$$

and $A_{F,m} \Phi_{mN}$ approaches

$$
A_{F,m} \Phi_{mN} = A_{F,m} \frac{1}{F} \hat{\Phi}_{mN}^F ([\exp(-j2\pi f t)]^F)^*. \tag{29}
$$

After the temporal reduction, Eq. (25) is equivalent to

$$
\hat{\Phi}_{mN}^F [j2\pi f]^F = A_{F,m} \hat{\Phi}_{mN}^F, \tag{30}
$$

which is a matrix system of $N \times F$ equations and $N \times N$ unknowns. Depending on the value of F, the system is over-determined ($F > N$), determined ($F = N$) or under-determined ($F < N$). In the first and last cases, the solution is taken in a least-squares sense, using the pseudo-inverse [47] of $\hat{\Phi}^F_{mN}$:

$$A_{F,m} = \hat{\Phi}^F_{mN}[j2\pi f]^F(\hat{\Phi}^F_{mN})^{-1}_{\mathrm{PI}}, \tag{31}$$

where PI stands for pseudo-inverse.

The question then arises of which Fourier modes of $\hat{\Phi}_{mN}$ should be retained. In order to minimize the truncation error based on an energy norm, such as the Fröbenius norm, the choice should be based on the energy of the Fourier modes, i.e., on their PSD. Other more sophisticated criteria are also possible, which may lead to more efficient temporal ROMs in certain cases. For example, if the energy spectrum contains peaks which are broad, with various frequencies associated to each peak, one may select only one frequency per peak, corresponding to the one with highest energy. This way the peaks will be approximately captured, and the number of Fourier modes can be highly reduced. If, on the other hand, the peaks in the energy spectrum are sharp, with only one frequency associated to each peak, this method will be close to the energy criterion described above. As in the present study the ROMs are evaluated through an energy norm (Fröbenius norm), only the energy criterion has been considered. This temporal ROM will be called t-ROM from now on. From an information point of view, t-ROM reduces a matrix of size $N \times S$ to a matrix of size $N \times N$. Note that a t-ROM is obtained for each azimuthal number m.

The t-ROM is integrated in time in order to determine its solutions. The analytical solution of a linear differential system with constant coefficients is well known:

$$\{\Phi_{mn}\}(t) = \sum_{l=1}^{l=N} C_{ml}\exp(\lambda_{ml}t)\{v_{ml}\}, \tag{32}$$

where (λ_{ml}, v_{ml}) are the eigenvalue–eigenvector pairs of the matrix $A_{F,m}$, and C_{ml} are the modal weights. The latter are determined from a best-fit between the analytical solution and Φ_{mN}.

The stability of t-ROM is determined by the real parts of the eigenvalues λ_{ml}. In this case, the real parts are close to zero for all the cases tested, even for the largest reductions. Furthermore, imposing purely imaginary eigenvalues when integrating t-ROM leads to the same solutions than when the real parts are left free. Therefore, t-ROM appears to prevent temporal instabilities, which can be problematic in other types of temporal ROM, such as ROMs based on DMD [13,14] or ROMs determined by a least-squares fit in the time domain [17]. The reason that the real parts are close to zero is that t-ROM is built from Fourier modes. The stability of t-ROM appears to be general; it applies to any choice of flow variables, spatial region, sampling parameters, etc. Figure 25a shows the Ritz values corresponding to the chronos-DMD and the current approach, for the case $N = F = N_{DMD} = 100$. In both cases, they lie in the vicinity of the unit circle (dashed line). Figure 25b shows the corresponding eigenvalues. While chronos-DMD leads to slightly unstable modes and large reconstruction errors, t-ROM leads to marginally stable modes and accurate reconstructions of the dataset. However, a better performance of chronos-DMD is recognized in the case that the entire chronos basis is

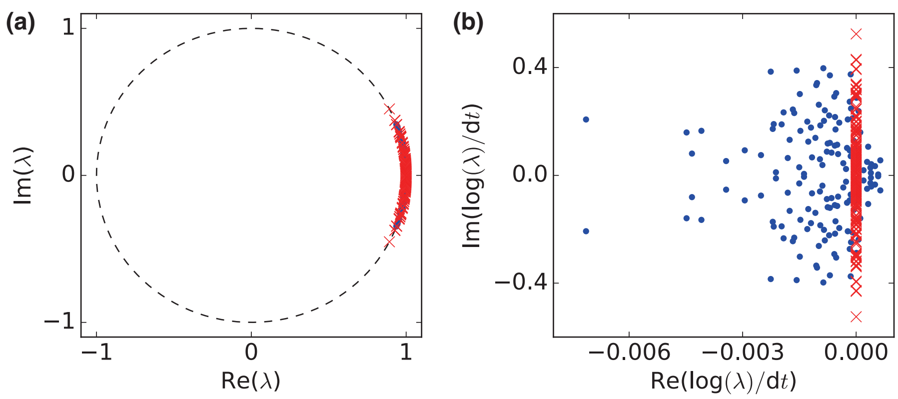

Fig. 25 **a** Ritz values and **b** eigenvalues from t-ROM (crosses) and from the chronos-DMD method [16] (circles), for $N = F = N_{DMD} = 100$

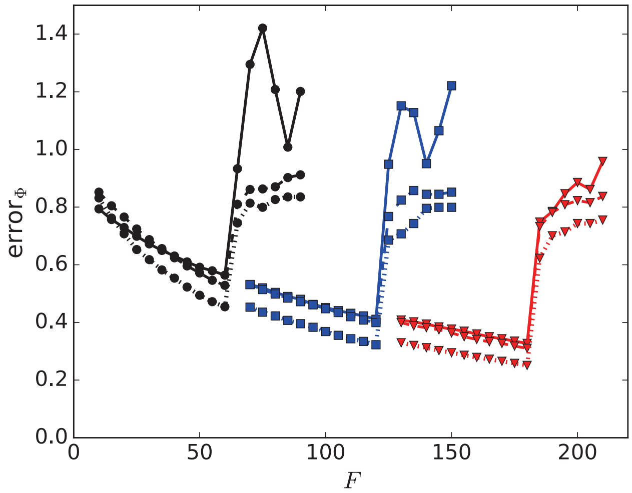

Fig. 26 Error of t-ROM as a function of the number of retained Fourier modes, for chronos basis of size $N = 60$ (circles), $N = 120$ (squares) and $N = 180$ (gradients), corresponding to $m = 0$ (solid), $m = 1$ (dashed) and $m = 2$ (dotted) results

used for computing the dynamic modes, for equal number of dynamic modes and Fourier modes retained, i.e., $N = S$ and $N_{DMD} = F$.

In the case that t-ROM is integrated from artificial initial conditions, they should not be arbitrarily determined. For $m = 0$, the paired POD modes describing the same convecting structure (Sect. 4.2.3) need to be in quarter-phase. For $m > 0$, the POD modes are complex and it is the real and imaginary parts of the POD modes describing a convecting structure which need to be in quarter-phase.

5.3 Evaluation of the temporal ROM

The performance of t-ROM as a function of the number of Fourier modes retained is shown in Fig. 26. The best performance of t-ROM is obtained when $F = N$. It deteriorates fast for increasing F, and more gradually for decreasing F. The size of t-ROM is equivalent to the size of $A_{F,m}$, which is $N \times N$, independent of the number of Fourier modes retained. For a given number of chronos, adding Fourier modes in t-ROM means fitting more information in the matrix $A_{F,m}$, of size $N \times N$, and thus implies increasing the error. On the other hand, diminishing the number of Fourier modes implies using less information to describe a same chronos basis, and the error also increases.

The reconstructed solutions from t-ROM are shown in Fig. 27a, b, and compared with the original 1st and 10th chronos. The corresponding frequency spectra (without the predicted portion) are shown in Fig. 28a, b. All correspond to 2078 snapshots ($S = 2078$) and a basis of 60 chronos ($N = 60$), the various curves corresponding to different sizes of the Fourier basis. The leading chronos (ϕ_1) has a lower frequency content than the 10th chronos (ϕ_{10}), and thus, it requires a smaller Fourier basis to be approximated. Increasing the size of the Fourier basis essentially ameliorates the temporal reconstruction at higher frequencies, and does not really improve the reconstruction at low frequencies.

5.4 Evaluation of the spatiotemporal ROM

In the following, the performance of the complete spatiotemporal ROM as a function of the number of POD modes retained is analyzed, for the particular case where $F = N$. This choice clearly leads to the optimum performance of t-ROM. Figure 29a, b shows the variation of the temporal reduction error (error_Φ), the spatial reduction error ($\text{error}_{\text{POD}}$) and the total error ($\text{error}_{\text{ROM}}$), for (a) $m = 0$ and (b) $m = 1$. The spatial reduction error is lower than the temporal reduction error, which is not surprising since the POD is the optimal decomposition, while the Fourier decomposition is only optimal in the ideal case of infinitely large times. Table 4 highlights the reduction achievable by the spatiotemporal ROM in terms of the size of the POD basis (spatial reduction) and the Fourier basis (temporal reduction). The low-pass temporal filter applied prior to

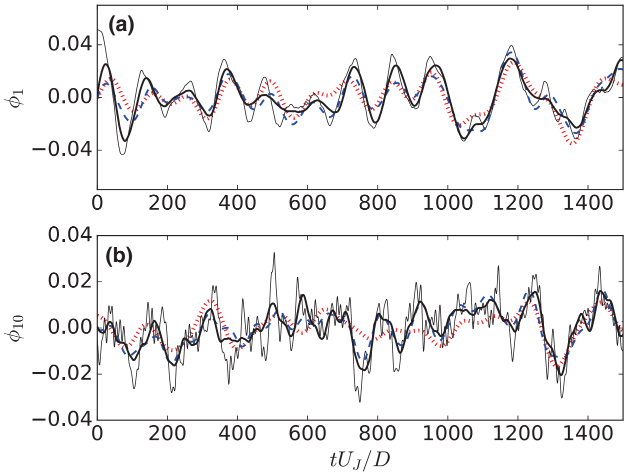

Fig. 27 Reconstructed time signals (real part) from the $m = 1$ t-ROM with $S = 2078$, corresponding to the **a** 1st and **b** 10th chronos for $N = 60$ (thin solid line: original chronos; dotted line: $F = 20$; dashed line: $F = 40$; thick solid line: $F = N = 60$)

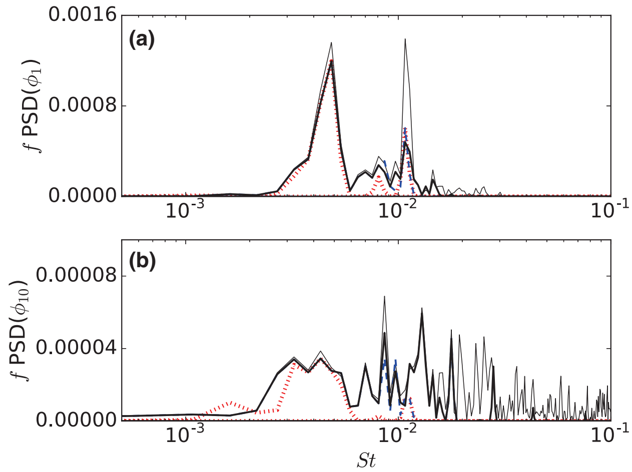

Fig. 28 Reconstructed spectra from $m = 1$ t-ROM with $S = 2078$, corresponding to the **a** 1st and **b** 10th chronos for $N = 60$ (thin solid line: original chronos; dotted line: $F = 20$; dashed line: $F = 40$; thick solid line: $F = N = 60$)

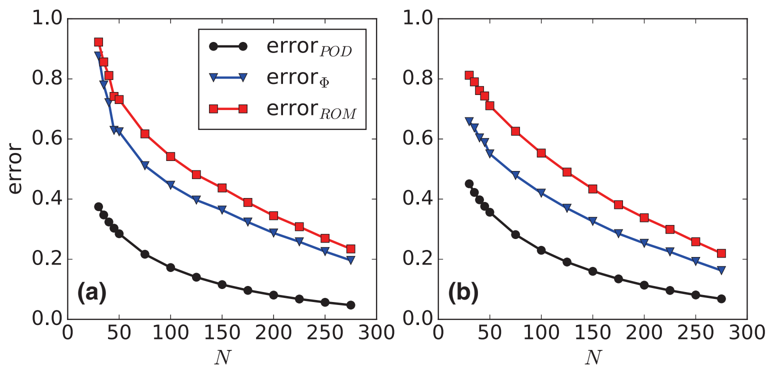

Fig. 29 Error of t-ROM (error$_\Phi$), the POD reconstruction (error$_{\mathrm{POD}}$) and the full spatiotemporal ROM (error$_{\mathrm{ROM}}$), corresponding to **a** $m = 0$ and **b** $m = 1$, for the case $F = N$

Table 4 Size decrease by the successive reductions (the error is computed with respect to the filtered flow field, so the error induced by the low-pass filter is 0)

	Error	M	N	F
No reduction	0	18	2078	2078
Low-pass filter ($\mathrm{St_{filt}} = 0.4\mathrm{St_{Nyq}}$)	0	18	570	830
Azimuthal truncation	0.2	6	570	830
	0.4	3	570	830
POD truncation	0.3	6	197	830
	0.6	6	22	830
POD truncation + t-ROM	0.3	6	230	230
	0.6	6	80	80

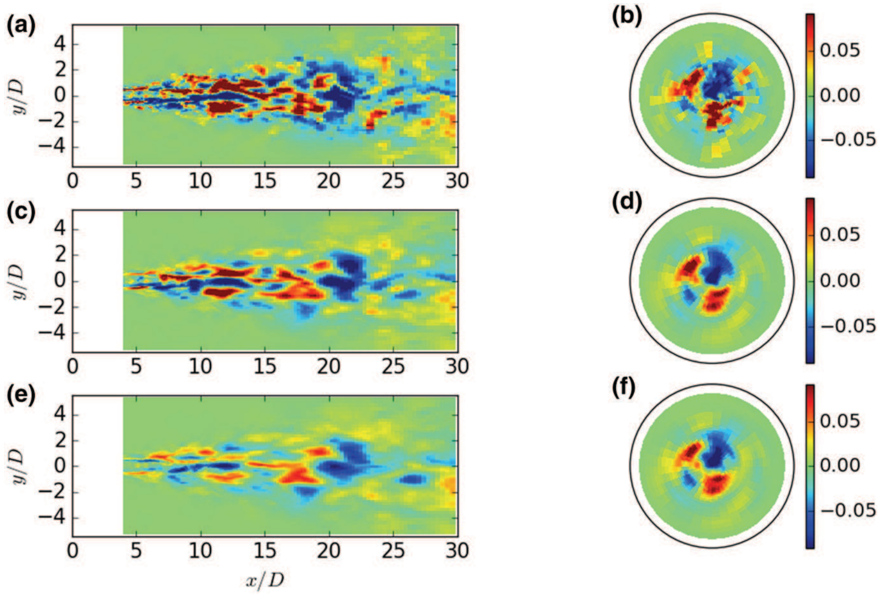

Fig. 30 **a, b** Unsteady axial velocity snapshot (taken after $1500D/U_J$), **c, d** reconstruction corresponding to the spatial reduction with $N = 80$ POD modes and $M = 6$ azimuthal modes, and **e, f** reconstruction corresponding to the spatiotemporal reduction with $N = 80$ POD modes, $M = 6$ azimuthal modes and $F = 80$ Fourier modes (all normalized by the reference velocity, U_J)

POD removes already a large portion of the high-frequency, small-scale energy in the flowfield. The starting 2078 POD modes (equal to the number of snapshots) and 2078 Fourier modes corresponding to the unfiltered and unreduced case are effectively reduced to about 570 POD modes and 830 Fourier modes. This number of POD modes has been estimated from the POD energies (Fig. 20a). The number of Fourier modes is simply 40% of 2078, corresponding to the filter cutoff frequency (40% of the Nyquist frequency). From here, the spatiotemporal ROM further reduces in space and in time, at the price of decreasing the accuracy of the reconstructed fields. Firstly, the number of azimuthal modes can be reduced, without decreasing the size of the POD or Fourier bases. With the leading 6 azimuthal modes, the error is limited to 20%, and with only 3 azimuthal modes, the error is 40%. Secondly, the size of the POD basis can be reduced, without reducing the Fourier basis. A POD basis of size 197 leads to an error of 30%, while a POD basis of 22 modes leads to an error of 60%. Finally, the reduction can be achieved by diminishing the size of the Fourier basis, while simultaneously diminishing the POD basis (we focus to the case $F = n$). Then, limiting the Fourier basis size to 230 gives an error of 30%, while a Fourier basis size of 80 leads to an error of 60%. In all cases, the lower the allowed error is, more modes are needed and the reduction is lower. As for any reduced model, there must be a compromise between the accuracy and the amount of reduction.

The reconstruction using the full spatiotemporal ROM of a $m = 0$ snapshot of the axial velocity and the temperature can be observed in Figs. 10c and 11c, respectively. The temporal reduction further eliminates the small structures of the axial velocity, leaving a clear large-scale pattern in the vicinity of the jet axis. Also, the spatial peak values are somewhat attenuated. The effect of the temporal reduction on the temperature is analogous.

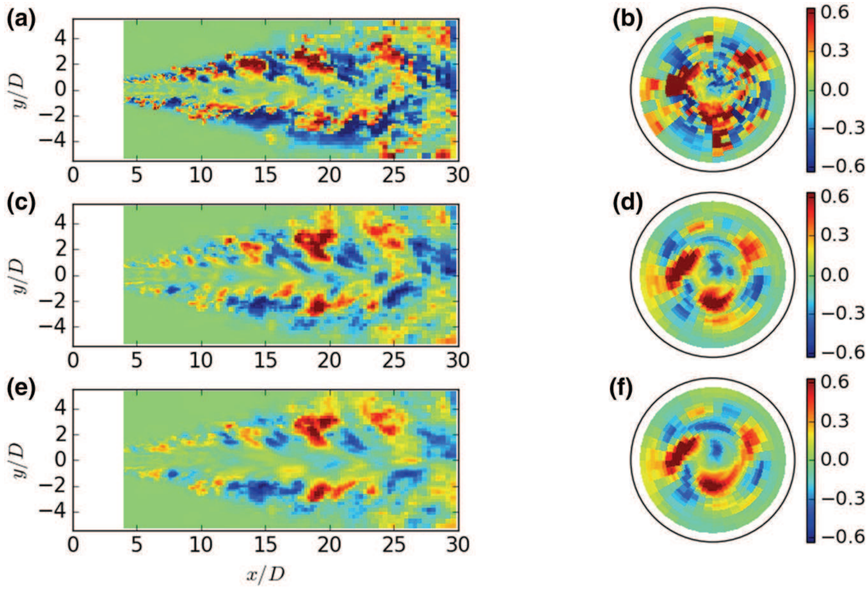

Fig. 31 **a, b** Unsteady temperature snapshot (taken after $1500D/U_J$), **c, d** reconstruction corresponding to the spatial reduction with $N = 80$ POD modes and $M = 6$ azimuthal modes, and **e, f** reconstruction corresponding to the spatiotemporal reduction with $N = 80$ POD modes, $M = 6$ azimuthal modes and $F = 80$ Fourier modes (all normalized by the reference temperature, T_J)

Examples of a reconstructed axial velocity snapshot and a temperature snapshot from the spatiotemporal ROM, corresponding to the ensemble of azimuthal modes, are shown in Figs. 30 and 31, respectively. The original unfiltered snapshots (a, b) are compared with the reconstructed snapshots corresponding to the spatial reduction retaining 80 POD modes and 6 azimuthal modes (c, d), and with the full spatiotemporal reduction retaining 80 POD modes, 6 azimuthal modes and 80 temporal Fourier modes (e, f). The main effects of the temporal low-pass filter plus the spatial reduction are a decrease in the amplitude of the peaks and the filtering of the small structures, associated to the lowest energy modes. The large structures remain approximately unchanged. Finally, the temporal reduction appears to have a somewhat stronger impact on the axial velocity field than on the temperature field, which is actually due to the fact that the most intense structures of the velocity are closer to the jet axis than the temperature structures, where the mean convection speed is higher and the active frequencies are also higher.

Finally, some details concerning the computational requirements of the present ROM are given. The data matrices of each of the 9 flow variables take about 3.9 Gb of hard disk space, while the individual POD modes take about 2Mb. For the extended set of variables, the total computation time in a personal computer with a processor of 2.8 GHz and 4 Gb of RAM is 25 min. This includes the temporal filter, the computation of the total energies of each variable (for the variable normalization), the azimuthal decomposition, the eigenvalue problem for each of the 19 azimuthal modes, the calculation of 120 topos for each of the 6 leading azimuthal modes and the computation of the temporal ROM with 120 Fourier modes for each of the 6 azimuthal modes.

6 Conclusions

A spatiotemporal ROM of a turbulent, reacting, over-expanded supersonic jet based on POD (spatial reduction) and a Fourier selection (temporal reduction) has been presented and assessed.

Due to the large set of variables included in the decomposition, the large region considered, and the high Reynolds number, the total fluctuating energy of the jet is distributed among a large number of POD modes. This leads to a relatively large POD basis required for an accurate reconstruction. The most energetic coherent structures of the jet have been shown to be an axisymmetric ($m = 0$) pulsation associated to the shock cells, and convected structures which are approximately wave packets at $m = 0$ and $m = 1$. The inclusion of a number of mass fractions in the decomposition changes the order of the leading modes, but their spatiotemporal structure is similar. The impact of the mass fractions on the energy distribution among the POD modes is remarkably weak. The strong cross-correlations of the mass fractions with the temperature explain this fact.

Finally, the temporal reduction has been achieved by a selection of the most energetic Fourier modes of the leading chronos, followed by a least-squares fitting into a homogeneous linear system. The resulting spatiotemporal ROM is general in nature: it can be applied to any stationary flow, with an arbitrary number of physical variables. Also, spatial symmetries can be easily exploited by performing a Fourier transform along the coordinates prior to the POD. Future perspectives certainly include the improvement of the flame through a subgrid-scale model for the chemistry, a mesh refinement in the vicinity of the jet lip line to capture the transition to turbulence in the shear layer further upstream [21], and the development of a systematic approach to the choice of variables, the region of analysis and a more efficient selection of POD modes in the periodic directions.

Acknowledgements This work has been funded by the ONERA internal project PRF SIMBA. The authors would like to thank Aurélien Guy and Sidonie Lefebvre for a number of useful comments and suggestions.

References

1. Caraballo, E., Samimy, M., Scott, J., Narayanan, S., DeBonis, J.: Application of proper orthogonal decomposition to a supersonic axisymmetric jet. AIAA J. **41**(5), 866–877 (2003)
2. Zhou, X., Hitt, D.L.: Proper orthogonal decomposition analysis of coherent structures in simulated reacting buoyant jets. AIAA J. **49**(5), 945–952 (2011)
3. Nobach, H., Tropea, C., Cordier, L., Bonnet, J.-P., Delville, J., Lewalle, J., Farge, M., Schneider, K., Adrien, R.: Handbook of experimental fluid mechanics. Chapter 22: Review of Some Fundamentals of Data Processing. Springer (2007)
4. Gudmundsson, K., Colonius, T.: Instability wave models for the near-field fluctuations of turbulent jets. J. Fluid Mech. **689**, 97–128 (2011)
5. Davoust, S., Jacquin, L., Leclaire, B.: Dynamics of m=0 and m=1 modes of streamwise vortices in a turbulent axisymmetric mixing layer. J. Fluid Mech. **709**, 408–444 (2012)
6. Rowley, C.W., Colonius, T., Murray, R.M.: Model reduction for compressible flows using pod and galerkin projection. Phys. D Nonlinear Phenom. **189**, 115–129 (2004)
7. Rempfer, D.: On low-dimensional galerkin models for fluid flow. Theor. Comput. Fluid Dyn. **14**, 75–88 (2000)
8. Couplet, M., Sagaut, P., Basdevant, C.: Intermodal energy transfers in a proper orthogonal decomposition-galerkin representation of a turbulent separated flow. J. Fluid Mech. **491**, 275–284 (2003)
9. McKeon, B.J., Sharma, A.S.: A critical-layer framework for turbulent pipe flow. J. Fluid Mech. **658**, 336–382 (2010)
10. Gomez, F., Blackburn, H.M., Rudman, M., Sharma, A.S., McKeon, B.J.: A reduced-order model of three-dimensional unsteady flow in a cavity based on the resolvent operator. J. Fluid Mech. **798**, 408–444 (2016)
11. Beneddine, S., Yegavian, R., Sipp, D., Leclaire, B.: Unsteady flow dynamics reconstruction from mean flow and point sensors: an experimental study. J. Fluid Mech. **824**, 174–201 (2017)
12. Beneddine, S., Sipp, D., Arnault, A., Dandois, J., Lesshafft, L.: Conditions for validity of mean flow stability analysis. J. Fluid Mech. **798**, 485–504 (2016)
13. Schmid, P.J.: Dynamic mode decomposition of numerical and experimental data. J. Fluid Mech. **656**, 5–28 (2010)
14. Rowley, C.W., Mezic, I., Bagheri, S., Schlatter, P.: Spectral analysis of nonlinear flows. J. Fluid Mech. **641**, 115–127 (2009)
15. Chen, K.K., Tu, J.H., Rowley, C.K.: Variants of dynamic mode decomposition: boundary condition, Koopman, and Fourier analyses. J. Nonlinear Sci. **22**(6), 887–915 (2012)
16. Cammilleri, A., Gueniat, F., Carlier, J., Pastur, L., Memin, E., Lusseyran, F., Artana, G.: POD-spectral decomposition for fluid flow analysis and model reduction. Theor. Comput. Fluid Dyn. **27**(6), 787–815 (2013)
17. Perret, L., Collin, E., Delville, J.: Polynomial identification of pod based low-order dynamical system. J. Turbul. **7**, 1–15 (2006)
18. Berkooz, G., Holmes, P., Lumley, J.L.: The proper orthogonal decomposition in the analysis of turbulent flows. Annu. Rev. Fluid Mech. **25**, 539–575 (1993)
19. Duwig, C., Iudiciani, P.: Extended proper orthogonal decomposition for analysis of unsteady flames. Flow Turbul. Combust. **84**, 25–47 (2010)
20. Rialland, V., Guy, A., Gueyffier, D., Perez, P., Roblin, A., Smithson, T.: Numerical simulation of ionized rocket plumes. J. Phys. Conf. Ser. **676**(–), 1–12 (2016)
21. Langenais, A., Vuillot, F., Troyes, J., Bailly, C.: Numerical investigation of the noise generated by a rocket engine at lift-off conditions using a two-way coupled cfd-caa method. In: 23th AIAA/CEAS Aeroacoustics Conference, Denver, Colorado, June 2017. AIAA, pp. 25–47 (2017)
22. Gueyffier, D., Fromentin-Denoziere, B., Simon, J., Merlen, A., Giovangigli, V.: Numerical simulation of ionized rocket plumes. J. Thermophys. Heat Transf. **28**(2), 218–225 (2014)
23. Guy, A., Fromentin-Denoziere, B., Phan, H-K., Cheraly, A., Gueyffier, D., Rialland, V., Erades, C., Elias, P.Q., Labaune, Jarrige, J., Ristori, A., Brossard, C., Rommeluere, S.: Ionized solid propellant rocket exhaust plume: miles simulation and comparison to experiment. In: 7th European Conference for Aeronautics and Space Sciences (EUCA SS), Milan, Italy, July 2017. EUCASS Association, pp. 1–19 (2017)
24. Refloch, A., Courbet, B., Murrone, A., Villedieu, P., Laurent, C., Gilbank, P., Troyes, J., Tessé, L., Chaineray, G., Dargaud, J.B., Quémerais, E., Vuillot, F.: Cedre software. AerospaceLab **1**(2), 1–10 (2011)
25. LeTouze, C., Murrone, A., Guillard, H.: Multislope muscl method for general unstructured meshes. J. Comput. Phys. **284**, 389–418 (2015)

26. Toro, E.F., Spruce, M., Speares, W.: Restoration of the contact surface in the HLL-Riemann solver. Shock Waves **4**, 25–34 (1994)
27. Gao, F., O'Brien, E.E.: A large-eddy simulation scheme for turbulent reacting flows. Phys. Fluids A Fluid Dyn. **5**(6), 1282–1284 (1993)
28. Jimenez, J., Linan, A., Rogers, M.M., Higuera, F.J.: A priori testing of subgrid models for chemically reacting non-premixed turbulent shear flows. J. Fluid Mech. **349**, 149–171 (1997)
29. DesJardin, P.E., Frankel, S.H.: Large eddy simulation of a non-premixed reacting jet: application and assessment of subgrid-scale combustion models. Phys. Fluids **10**(9), 2298–2314 (1998)
30. Celik, I., Cehreli, Z., Yavuz, I.: Index of resolution quality for large eddy simulations. ASME J. Fluids Eng. **127**, 949–958 (2005)
31. Pack, D.C.: A note on prandtl's formula for the wave-length of a supersonic gas jet. Q. J. Mech. Appl. Math. **3**(2), 173–181 (1950)
32. De Cacqueray, N., Bogey, C., Bailly, C.: Investigation of a high-mach-number over-expanded jet using large-eddy simulation. AIAA J. **49**(10), 2171–2182 (2011)
33. Brès, G.A., Jordan, P., Jaunet, V., Le Rallic, M., Cavalieri, A.V.G., Towne, A., Lele, S.K., Colonius, T., Schmid, O.T.: Importance of the nozzle-exit boundary-layer state in subsonic turbulent jets. J. Fluid Mech. **851**, 83–124 (2018)
34. Lorteau, M., Cléro, F., Vuillot, F.: Analysis of noise radiation mechanism in hot subsonic jet from a validated large eddy simulation solution. Phys. Fluids **27**, 075108 (2015)
35. Langenais, A., Vuillot, F., Troyes, J., Bailly, C.: Accurate simulation of the noise generated by a hot supersonic jet including turbulence tripping and nonlinear acoustic propagation. Phys. Fluids **31**, 016105 (2018)
36. Lumley, J.L.: Atmospheric Turbulence and Radio Wave Propagation: The Structure of Inhomogeneous Turbulent Flows. Nauka, Moscow (1967)
37. Taira, K., Brunton, S.L., Dawson, S.T.M., Rowley, C.W., Colonius, T., McKeon, B.J., Schmidt, O.T., Gordeyev, S., Theofilis, V., Ukeiley, L.S.: Modal analysis of fluid flows: an overview. AIAA J. **55**(12), 4013–4041 (2017)
38. Poje, A., Lumley, J.L.: Low-dimensional models for flows with density fluctuations. Phys. Fluids **9**(7), 2023–2031 (1997)
39. Deane, A.E., Kevrekidis, I.G., Karniadakis, G.E., Orszag, S.A.: Low-dimensional models for complex geometry flows: application to grooved channels and circular cylinders. Phys. Fluids A Fluid Dyn. **3**(10), 2337–2354 (1991)
40. Noack, B., Afanasiev, K., Morzyński, M., Tadmor, G., Thiele, F.: A hierarchy of low-dimensional models for the transient and post-transient cylinder wake. J. Fluid Mech. **497**, 335–363 (2003)
41. Crighton, D.G., Gaster, M.: Stability of slowly diverging jet flow. J. Fluid Mech. **77**(2), 397–413 (1976)
42. Michalke, A., Fuchs, H.V.: On turbulence and noise of an axisymmetric shear flow. J. Fluid Mech. **70**, 179–205 (1975)
43. Luo, K.H., Sandham, N.D.: Instability of vortical and acoustic modes in supersonic round jets. Phys. Fluids **9**(4), 1003–1013 (1997)
44. Jordan, P., Colonius, T.: Wave packets and turbulent jet noise. Annu. Rev. Fluid Mech. **45**, 173–195 (2013)
45. Schmidt, O.T., Towne, A., Rigas, G., Colonius, T., Brès, G.A.: Spectral analysis of jet turbulence. J. Fluid Mech. **855**, 953–982 (2018)
46. Towne, A., Schmid, O.T., Colonius, T.: Spectral proper orthogonal decomposition and its relationship to dynamic mode decomposition and resolvent analysis. J. Fluid Mech. **847**, 821–867 (2018)
47. Ben-Israel, A., Greville, T.N.E.: Generalized Inverses: Theory and Applications, 2nd edn. Springer, Berlin (2003)